Supporting Information

Conductive Organic Cages Enable Efficient Capture and Transistor Detection of ppq-Level Perfluorooctanoic Acid

Chao-Wang Tang,[1] Wen-Wen Wang,[1] Jing-Yan Tang,[2] Yixin Wang,[1,*] Yang-Yang Wang,[1] and Qiang Yan[1,*]

[1]*State of Key Laboratory of Molecular Engineering of Polymers, Fudan University, Shanghai 200433, China*

[2]*School of Chemistry & Chemical Engineering, Henan University of Science and Technology, Henan 471023, China*

Corresponding author email: yanq@fudan.edu.cn

Content

1. Materials, Methods and Synthetic Procedures.

Materials. Tetrathiafulvalene (TTF, TCI, 98%), 4-bromobenzaldehyde (Sigma, 99%), *tert*-tributyl phosphine tetrafluoroborate ($PtBu_3HBF_4$, TCI, 97%), cesium carbonate ($CsCO_3$, TCI, 97%), (*1R,2R*)-1,2-diaminocyclohexane (TCI, 98%), trifluoroacetic acid (TFA, Sigma, 99%), palladium acetate ($Pd(OAc)_2$, TCI, 97%), sodium borohydride ($NaBH_4$, Sigma, 99%), 4-(trifluoromethyl)benzoic acid (Sigma, 99%), perfluorooctanoic acid (PFOA, TCI, 99.7%), and hexafluorobenzene (HFB, TCI, 99.5%), were used as received. All solvents including methanol (CH_3OH), ethanol, tetrahydrofuran (THF), *n*-hexane, dichloromethane (CH_2Cl_2), chloroform ($CHCl_3$), and *N,N*-dimethyl formamide (DMF) were obtained from Sinopharm Chemical Reagent Co. Ltd. (Shanghai, China). Anhydrous solvents were purified using an Innovative Technologies Solvent Purification System and degassed prior to use by freeze-pump-thaw for two cycles. Aqueous solutions were prepared using Milli-Q water purification equipment (18 MΩ).

Methods. *Nuclear magnetic resonance (NMR)* spectroscopy was conducted on a Bruker AVANCE III HD 400 MHz NMR instrument to obtain ^{1}H NMR (400 MHz), ^{13}C NMR (101 MHz), and ^{19}F NMR (376MHz) spectra of all compounds and organic cages using CD_2Cl_2, CD_3OD, DMSO-d_6 or THF-d_8 as deuterium-labeling NMR solvents. *High-resolution electrospray ionization mass spectroscopy (HR-ESI-MS)* was recorded on a Bruker MicroTOF II mass spectrometer equipped with an ESI interface and ion trap analyzer for the characterization of *m*/*z* of the resulted organic cages. *Fourier transform infrared (FT-IR)* spectroscopy was measured on a Perkin-Elmer Spotlight 400 FT-IR system. The solid powders of the molecular cages (TTFcage and ReTTFcage) were respectively pressed in KBr pellets and then scanned at the range of 500~4000 cm^{-1} to obtain the IR curves. *Single crystal X-ray diffraction (SCXRD)* data were collected on a Bruker D8 VENTURE Metal-Jet X-ray diffractometer (Bruker, Germany) equipped with an APEX II detector. X-rays were generated by a Ga/In source (λ = 1.34139 Å), and the crystal was maintained at 193.00 K during data collection. The structure was solved using the SHELXT structure solution program with Intrinsic Phasing and refined

using the XL refinement package with Least Squares minimization in Olex2. *X-ray photoelectron spectroscopy (XPS)* was performed on a PHI Quantera-II system using monochromatic Al K_α X-ray sources (1486.6 eV). The adventitious carbon signal at 284.8 eV was used for calibration. *Powder X-ray diffraction (PXRD)* was conducted using a Bruker AXS D8 Advance diffractometer operated at 1,600 W power (40 kV, 40 mA) with Cu-K_α radiation. *Brunauer-Emmett-Teller (BET)* was analyzed using a BSD-PMC instrument through the multi-point method. The nitrogen adsorption-desorption isotherms were measured under a temperature of 77 K, and the pore size distribution (PSD) was derived from the data using non-local density functional theory (NLDFT) model for nitrogen adsorption. Before the adsorption measurements, the samples were activated by soaking the cage solid powders in methanol overnight to achieve solvent exchange and remove residual guest molecules, and then were conventionally heated at 120 °C for 24 h to ensure the open pore structure. *Cyclic voltammetry (CV)* measurements were performed on a CHI760E electrochemical workstation using a three-electrode configuration in 0.5 M Na_2SO_4 aqueous solution. The working electrode was a glassy carbon electrode modified with ReTTFcage. The potential window was −1 V to +1 V, and the scan rate was 50 mV s^{-1}. *Electrochemical impedance spectroscopy (EIS)* measurements were carried out on the same CHI760E workstation in 0.5 M Na_2SO_4 aqueous solution. The frequency range was 100 kHz to 0.1 Hz with an AC amplitude of 10 mV at the open-circuit potential. *Electron paramagnetic resonance (EPR)* data were measured on a Bruker EMXplus-6/1 system. *Transmission electron microscopy (TEM)* images were obtained using a Thermo Fisher Talos F200S G2 electron microscope at an acceleration voltage of 120 kV. Energy dispersive X-ray spectroscopy (EDX) was performed with the Talos at an acceleration voltage of 200 kV. The ReTTFcage dispersions in methanol (10 μL) were dropped onto the carbon-coated copper grids. After incubation for 2 min, excess solution was blotted from the grid and then immersed into liquid nitrogen (30 s) followed by freeze-dried process in vacuum before observation.

PFOA Quantitative Analysis. After the adsorption experiments using cage materials,

the quantitative analysis of the residual amount of PFOA or other PFAS was conducted by combining an ultra-high performance liquid chromatograph with a quadrupole ring trap mass spectrometer (UPLC-MS). Specifically, a Thermo Fisher Scientific's Thermo UPLC 3000 liquid chromatograph was used and connected to a Q Exactive plus mass spectrometer, for detecting various water samples containing PFOA. A Hypersil GOLD C18 column (2.1 mm × 100 mm, 3 μm) was employed for chromatographic separation at 25 °C. The mobile phase consisted of methanol (A) and 5 μM of aqueous acetic acid ammonium (B), and a gradient elution scheme was adopted. The flow rate of the mobile phase was set at 0.25 mL min^{-1}, and the injection volume was 10 μL. Mass spectrometry conditions: HESI ionization source, 40 nebulizer gas flow rates, 8 auxiliary gas flow rates, 3200 volts spray voltage, ion transmission capillary temperature of 300 °C. The auxiliary gas temperature was 280 °C; scanning mode: negative ion mode, scan range: *m*/*z*: 50~750. All data were collected and processed using Xcalibur 2.4 software.

Theoretical Calculation. The molecular calculations for the cage binding motifs with PFOA species were conducted using the Gaussian 16 program package. Code with the semiempirical tight-binding method GFN2-xTB, after obtaining proper initial guesses of the organic cage structure.[1,2] All calculations were carried out using Gaussian 16 at the density functional theory (DFT) level with the B3LYP[3] hybrid functional and the def2-SVP basis set. To precisely describe long-range dispersion interactions, Grimme's D3 dispersion correction with Becke-Johnson damping (D3BJ) was included. Solvent effects were treated implicitly via the self-consistent reaction field (SCRF) way. Single-point energy calculations were performed on the optimized geometries to evaluate the electronic energies.[4,5] The binding energy between the cage (ReTTFcage) and PFOA compound was calculated as the Eq.(1),

$$E = E_{PFOA@ReTTFcage} - \left(E_{ReTTFcage} + E_{PFOA}\right) \ldots\ldots\ldots\ldots (1)$$

where $E_{PFOA@ReTTFcage}$ represents the total energy of PFOA-cage complex, E_{PFOA} is the energy of free PFOA molecule, and $E_{ReTTFcage}$ as the energy of ReTTFcage itself. To further analyze the energy contributions of various noncovalent interactions between

ReTTFcage and PFOA, the B3LYP functional and def2-SVP basis set were used for energy decomposition analysis. The position of the hydrogen atom was optimized, and the other atoms keep their positions unchanged. The DFT-D3 dispersion correction with BJ-damping[6] was applied to correct the weak interaction to improve the calculation accuracy. Symmetry-adapted perturbation theory (SAPT) was performed to precisely analyze the physical nature of the intermolecular interactions at the sSAPT0/jun-ccpVDZ level.[7] SAPT analysis provides a decomposition of the interaction energy into physically meaningful components, such as electrostatics/H-bonding ($E_{elst/H}$), induction (E_{ind}), dispersion (E_{disp}), and exchange (E_{exch}) terms. The independent gradient model (IGM) based on the Hirshfeld partition method was employed using Multiwfn, with the geometries and electronic structures optimized at the GFN2-xTB level of theory. This method provides a detailed visualization and quantification of non-covalent interactions, such as hydrogen bonding and van der Waals forces, contributing to the affinity.[8]

Synthetic Procedure.

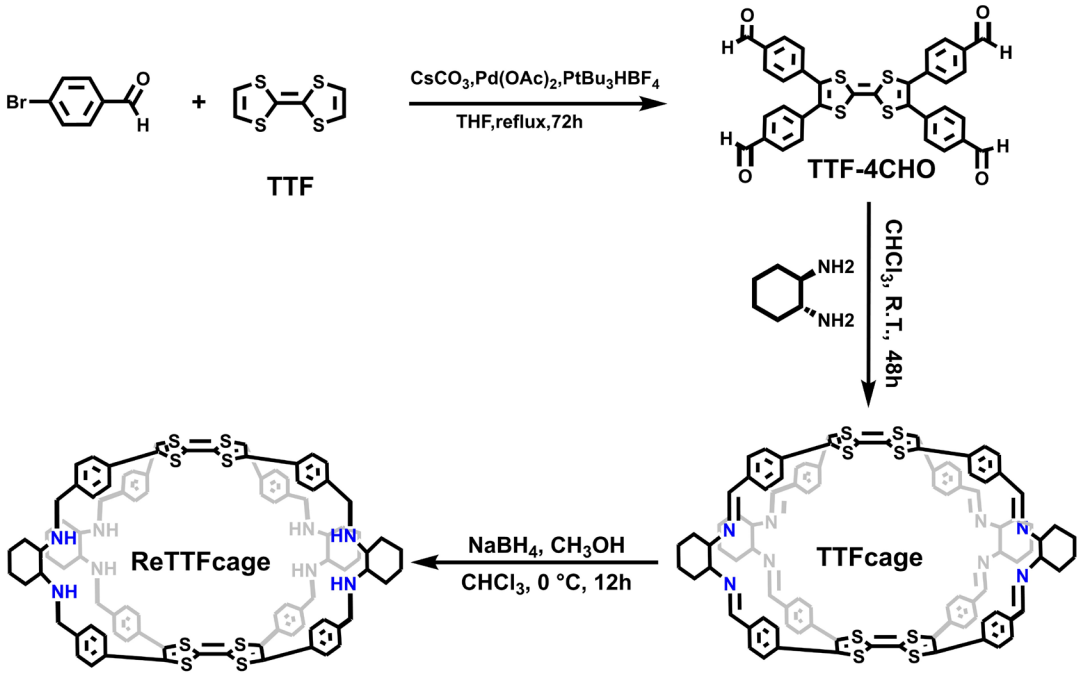

Scheme S1. Synthetic Route of ReTTFcage via Post-Modification.

Synthesis of TTF-containing compound (TTF-4CHO). A mixture of tetrathiafulvalene (TTF, 8.0 mmol, 1.63 g, 1.0 equiv.), 4-bromobenzaldehyde (40.0 mmol, 7.45 g, 5.0

equiv.), $Pd(OAc)_2$ (2.0 mmol, 0.45 g), $PtBu_3HBF_4$ (4.4 mmol, 1.74 g), and $CsCO_3$ (14.7 mmol, 9.63 g) dissolved in 80 mL of THF was degassed by freeze-pump-thaw cycles, and then purged with argon, and reflux for 72 h. The reaction mixture was subsequently extracted with chloroform (50 mL × 3), and the combined organic layers were washed with brine, dried over anhydrous sodium sulfate, and finally concentrated under reduced pressure. The product was purified by silica gel chromatography using acetone/CH_2Cl_2 (v/v, 3/500) as the eluent, affording a red-black solid TTF-4CHO (1.92 g, yield: 39%). ^{1}H NMR (400 MHz, δ, DMSO-d_6): 9.98 (s, 1H), 7.86 (d, J = 8.1 Hz, 2H), 7.47 (d, J = 7.3 Hz, 2H). ^{13}C NMR (101 MHz, δ, DMSO-d_6): 191.12, 137.86, 136.30, 130.23, 129.92, 129.76, 108.45. HR-ESI-MS: m/z for $C_{34}H_{20}O_4S_4$, $[M+H]^+$; found 620.0242 calcd. 620.0244 (***Figure S1-S3***).

Synthesis of TTF-based organic cage precursor (TTFcage). The TTFcage precursor was synthesized via Schiff-base reaction. Specifically, the resulted TTF-4CHO (0.25 g, 0.40 mmol, 1 equiv.) and catalytic amount of trifluoroacetic acid (5 μL) were dissolved in 50 mL of anhydrous $CHCl_3$. Subsequently, (*1R,2R*)-1,2-diaminocyclohexane (0.10 g, 0.89 mmol, 2.2 equiv.) was dissolved in 20 mL of $CHCl_3$ and added dropwise to the prepared solution. The mixture was stirred at room temperature for 48 h. Afterward, the mixture was filtered, and the filtrate was concentrated to 5 mL under reduced pressure. Finally, 100 mL of *n*-hexane was added, resulting in the rapid precipitation of an orange solid. Repeating this step for three times can consolidate the solid and obtain the product TTFcage (0.28 g, yield: 89%). ^{1}H NMR (400 MHz, δ, CD_2Cl_2): 7.75 (s, 4H), 7.66 (s, 4H), 7.42 (d, J = 8.5 Hz, 8H), 7.27 (d, J = 1.9 Hz, 8H), 7.05 (d, J = 8.3 Hz, 8H), 7.00 (d, J = 8.3 Hz, 8H), 3.24 (s, 4H), 3.15 (s, 4H), 2.29-1.76 (m, 32H). ^{13}C NMR (101 MHz, δ, CD_2Cl_2): 163.57, 161.65, 136.36, 135.98, 134.34, 133.76, 130.48, 130.24, 128.08, 127.60, 127.48, 127.36, 124.54, 123.52, 115.71, 73.79, 73.09, 32.14, 32.05, 31.58, 31.19, 29.89, 29.68, 24.48, 24.30, 22.64, 13.87, 0.75. HR-ESI-MS: m/z for $C_{92}H_{80}N_8S_8$, 1+ species, $[M+H]^+$; found 1553.4364, calcd. 1553.4344; 2+ species, $[M+2H]^{2+}$; found 777.2220, calcd. 777.2209 (***Figure S4-S6***).

Synthesis of target TTF-based organic cage via post-modification (ReTTFcage). The

above resulted TTFcage precursor (0.21 g, 0.13 mmol) was dissolved in a 100 mL of $CHCl_3$ and CH_3OH mixing solvent (v/v, 1/1). $NaBH_4$ (0.05 g, 1.30 mmol) was gradually added under an ice bath and the mixture was stirred for 12 h. Then 20 mL of water was added and reacted with stirring for 1 h. After the reaction ended, the filtrate was washed by water (50 mL × 3) and combined the organic layer, then dried with anhydrous sodium sulfate. The organic layer was concentrated to 5 mL under vacuum distillation and then *n*-hexane (100mL) was added to obtain a powder-like precipitation. After the mixture was filtered, the solid was collected and dried overnight at 80 °C, resulting in the orange target product, ReTTFcage (0.18 g, yield: 88%). ^{1}H NMR (400 MHz, δ, CD_2Cl_2): 7.38 (d, J = 2.4 Hz, 8H), 7.27 (dd, J = 8.4, 2.0 Hz, 8H), 7.12-7.06 (m, 8H), 6.99 (d, J = 5.9 Hz, 8H), 3.87 (d, J = 13.9 Hz, 3H), 3.69 (d, J = 13.3 Hz, 3H), 2.89-2.77 (m, 4H), 2.56 (t, J = 7.8 Hz, 4H), 2.06-1.90 (m, 32H). ^{13}C NMR (101 MHz, δ, CD_2Cl_2): 147.36, 145.74, 124.96, 124.72, 124.54, 123.93, 123.72, 123.52, 118.84, 118.66, 113.76, 64.48, 36.39, 34.09, 31.19, 29.88, 29.68, 25.91, 22.69, 13.88. HR-ESI-MS: *m*/*z* for $C_{92}H_{88}N_8S_8$, 1+ species, $[M+H]^+$; found 1569.5125, calcd. 1569.5569; 2+ species, $[M+2H]^{2+}$; found 785.2822, calcd. 785.2835 (***Figure S7-S9***).

2. Structural Characterization of ReTTFcage.

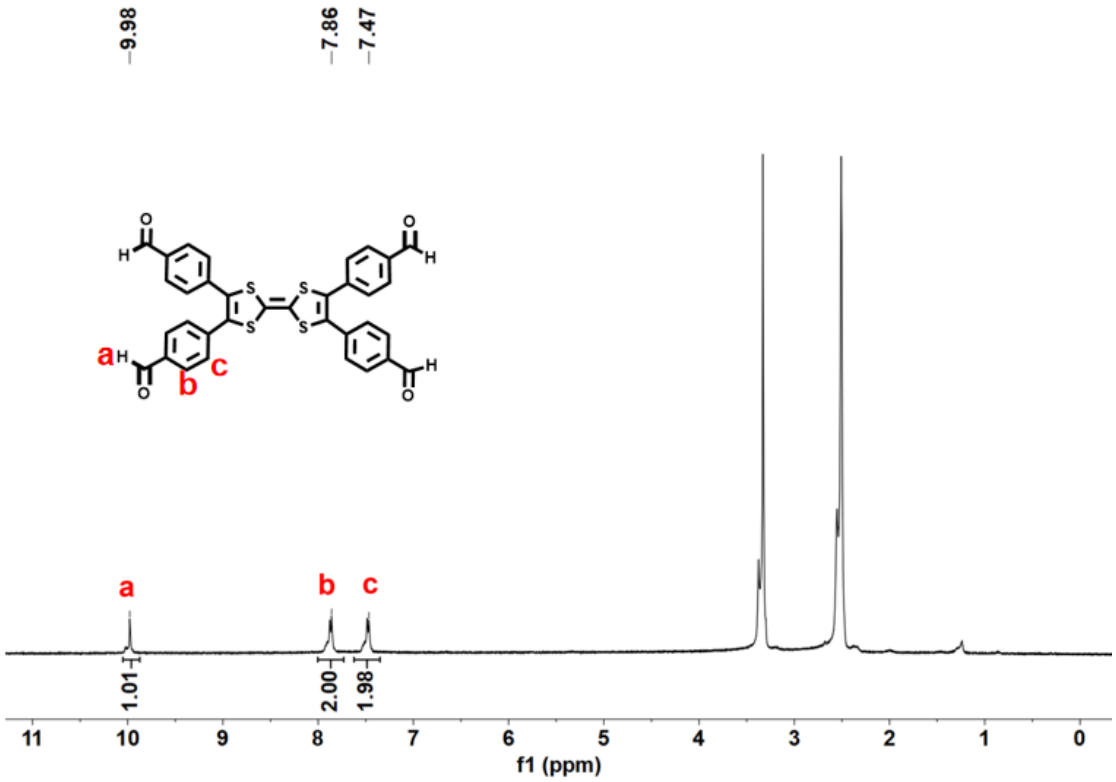

Figure S1. ^{1}H NMR spectrum of TTF-4CHO in DMSO-d_6.

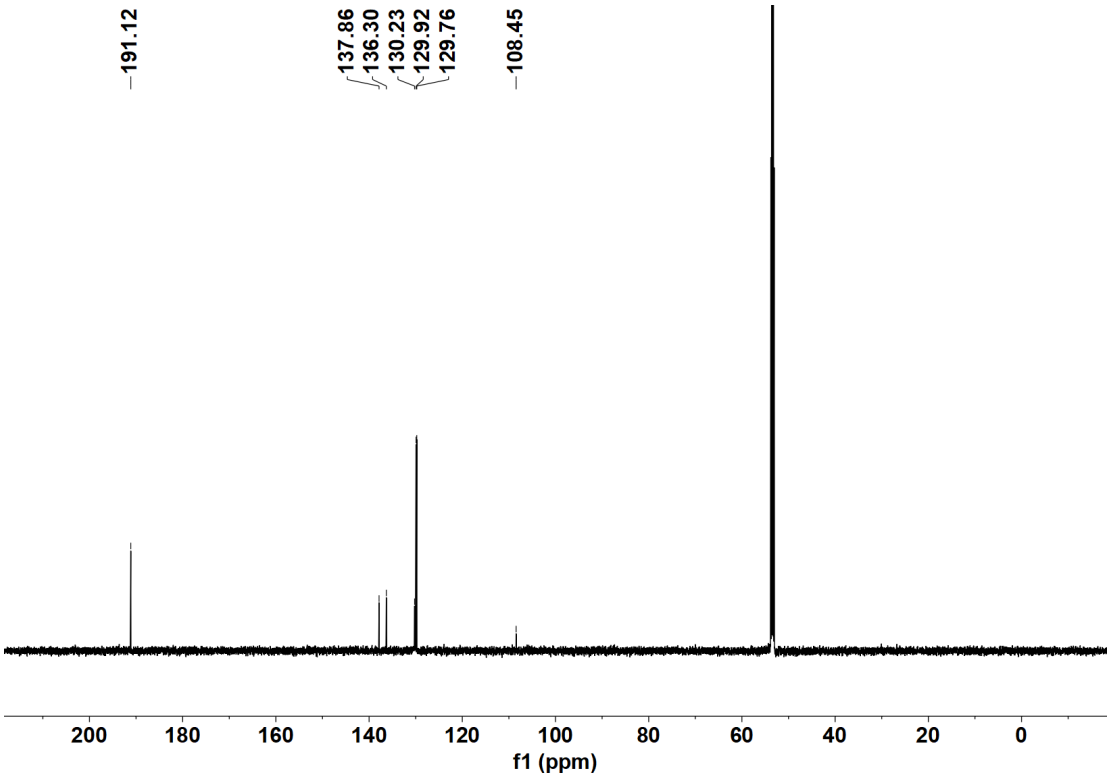

Figure S2. ^{13}C NMR spectrum of TTF-4CHO in DMSO-d_6.

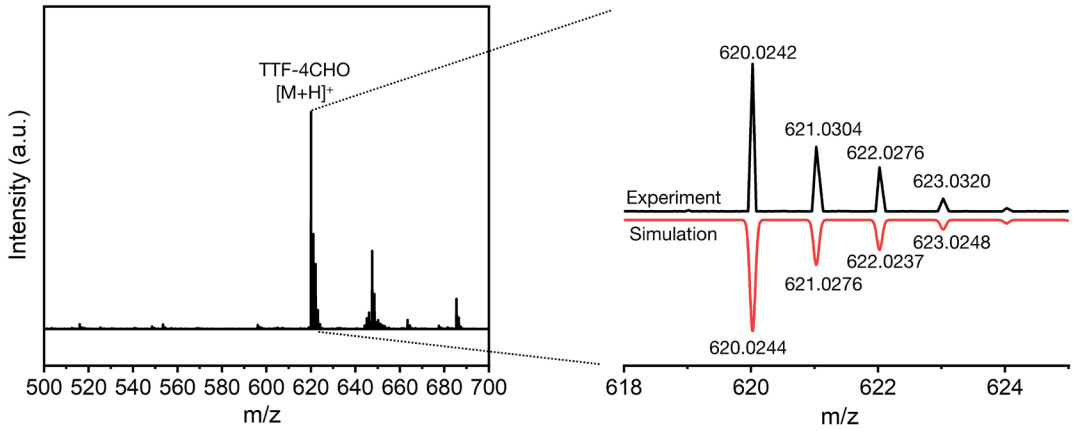

Figure S3. HR-ESI-MS spectrum of TTF-4CHO (*m/z* for $C_{34}H_{20}O_4S_4$, $[M+H]^+$; found 620.0242 calcd. 620.0244).

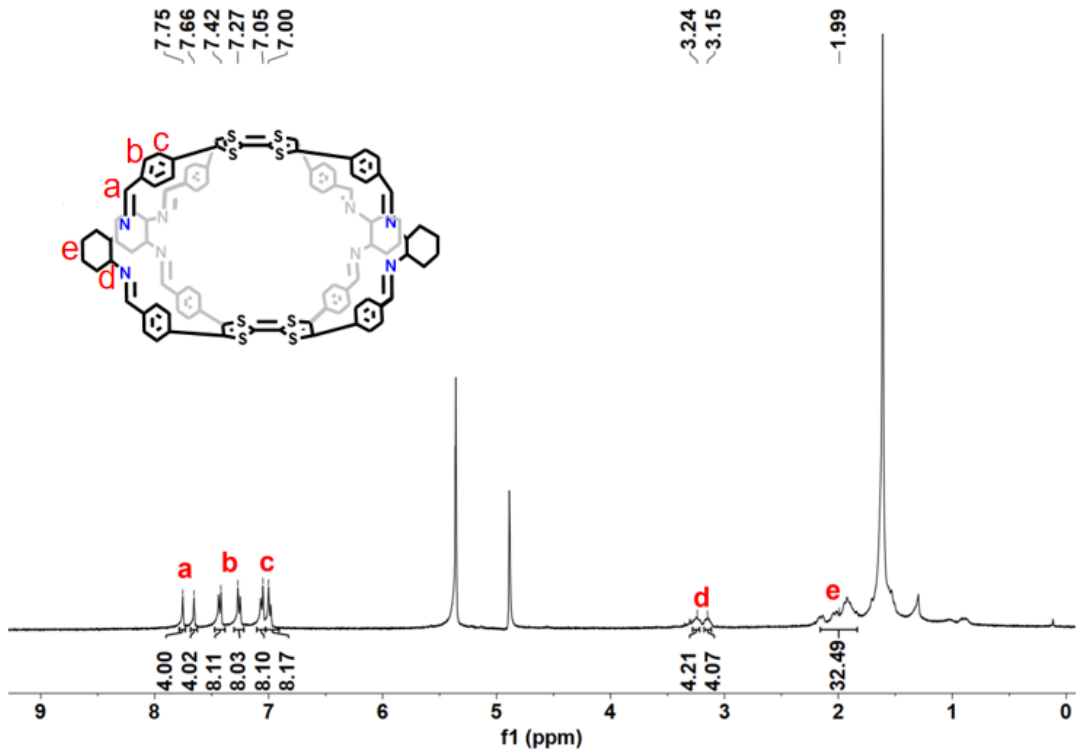

Figure S4. ^{1}H NMR spectrum of TTFcage precursor in CD_2Cl_2.

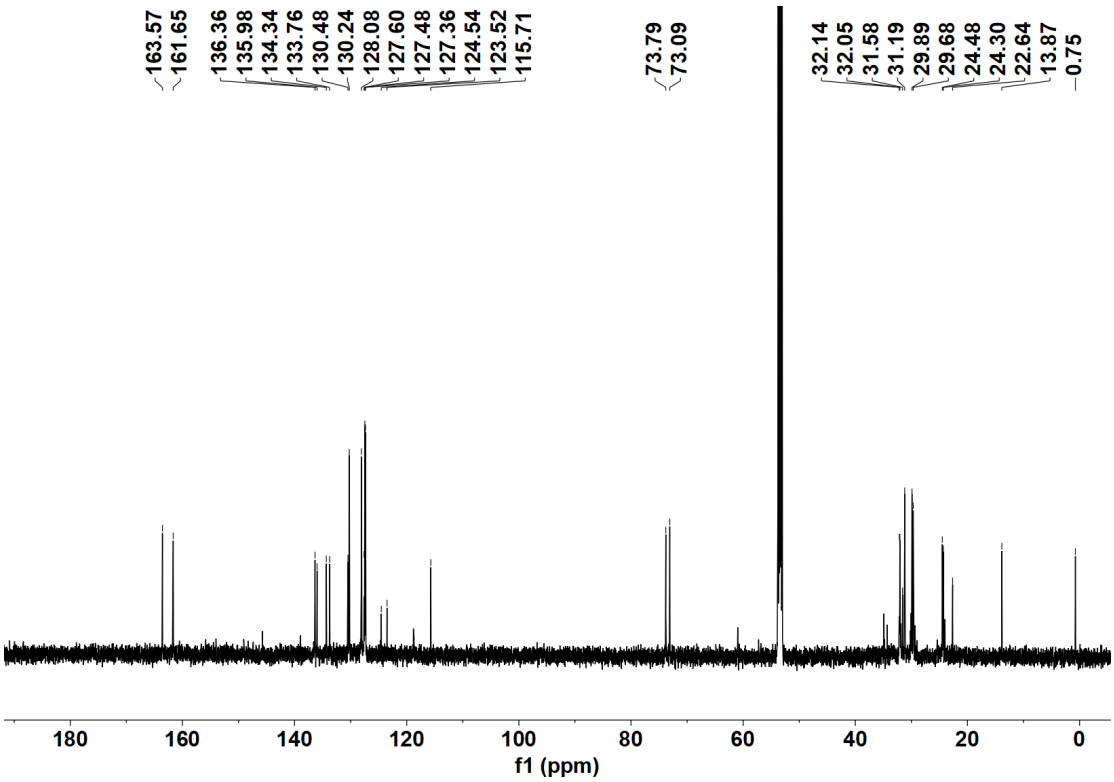

Figure S5. ^{13}C NMR spectrum of TTFcage precursor in CD_2Cl_2.

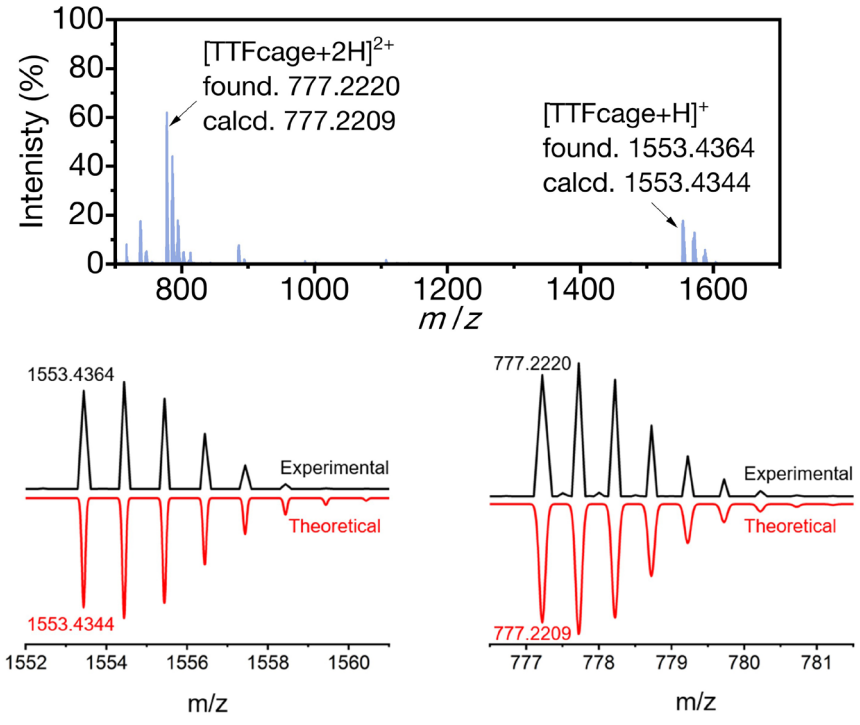

Figure S6. HR-ESI-MS spectrum of TTFcage precursor (*m/z* for $C_{92}H_{80}N_8S_8$, 1+ species, $[M+H]^+$; found 1553.4364, calcd. 1553.4344; 2+ species, $[M+2H]^{2+}$; found 777.2220, calcd. 777.2209).

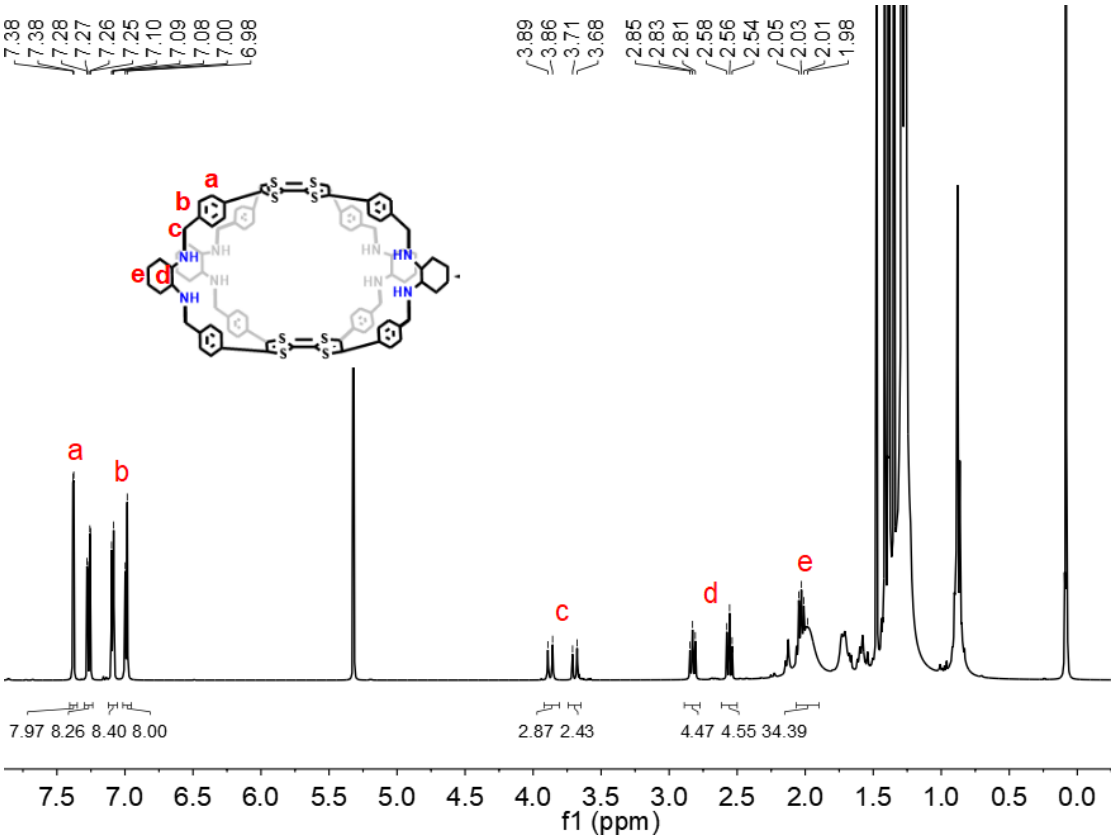

Figure S7. ^{1}H NMR spectrum of ReTTFcage in CD_2Cl_2.

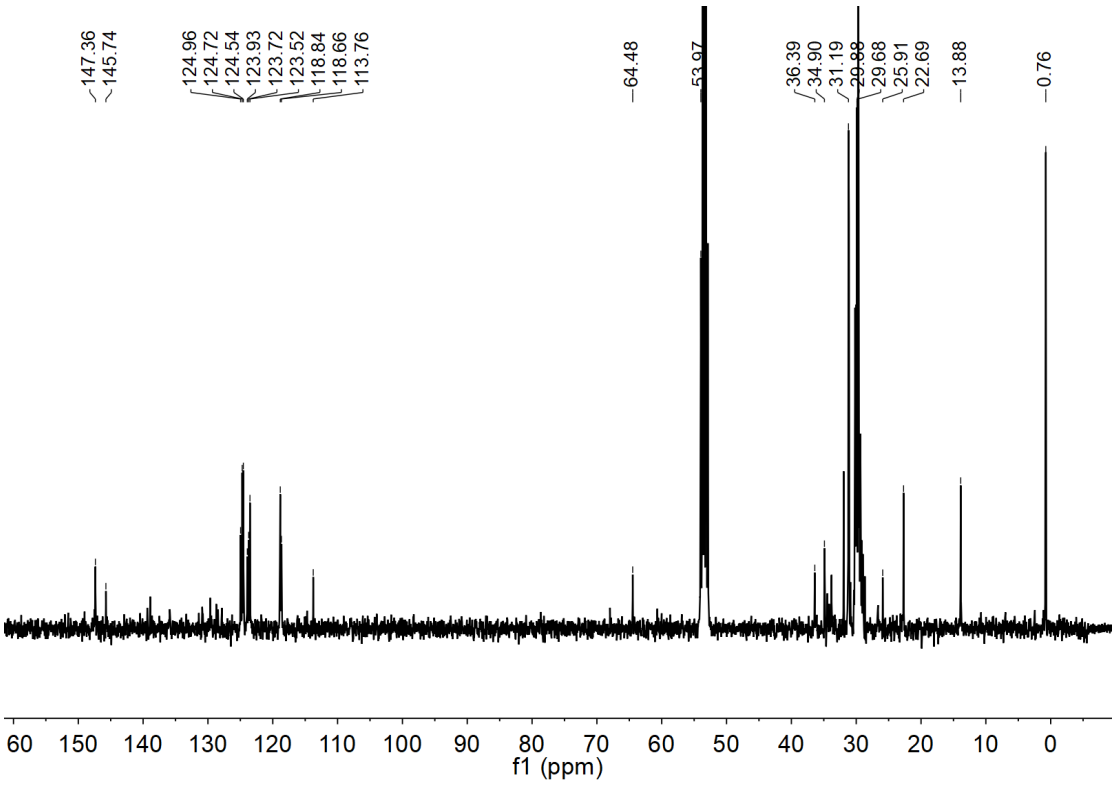

Figure S8. ^{13}C NMR spectrum of ReTTFcage in CD_2Cl_2.

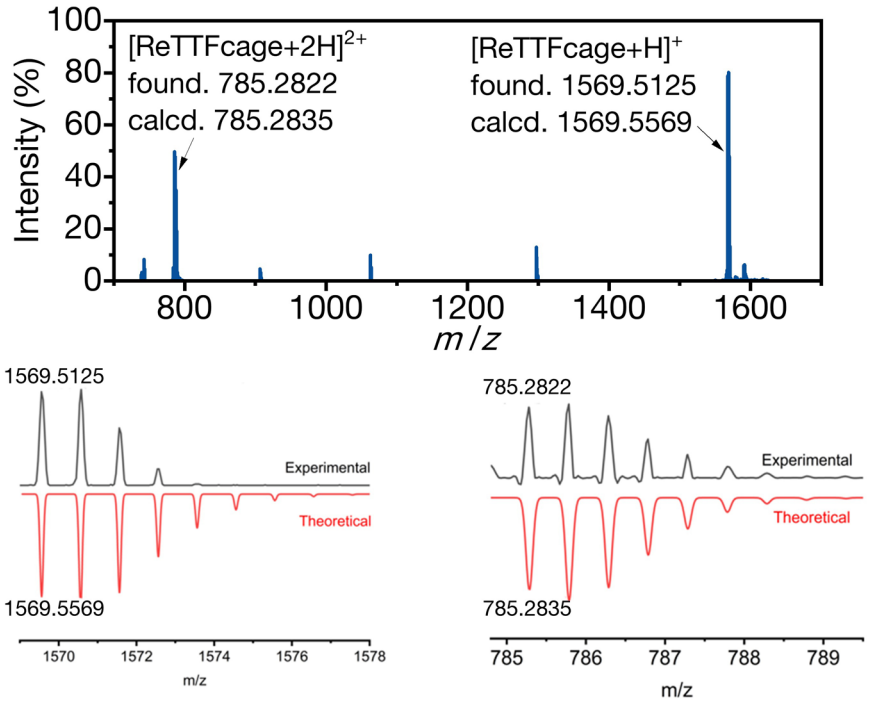

Figure S9. HR-ESI-MS spectrum of ReTTFcage (*m*/*z* for $C_{92}H_{88}N_8S_8$, 1+ species, $[M+H]^+$; found 1569.5125, calcd. 1569.5569; 2+ species, $[M+2H]^{2+}$; found 785.2822, calcd. 785.2835).

Table S1. Crystallographic data of the TTFcage obtained from $CHCl_3/CH_3OH$.

Empirical formula	$C_{205}H_{208}Cl_{36}N_{16}O_9S_{16}$
Formula weight	4829.02
Temperature	193.00 K
Wavelength	Ga Kα (λ = 1.34139 Å)
Crystal system	Monoclinic
Space group	$P2_1$
Unit cell dimensions	a = 12.0477(7) Å
	b = 28.2656(18) Å
	c = 17.9689(10) Å
	α = 90°
	β = 92.617(2)°
	γ = 90°
Volume	6112.7(6) $Å^3$
Z	1
Density (calculated)	1.312 g/cm^3
Absorption coefficient	3.564 mm^{-1}
F(000)	2490.0
Theta range for data collection	4.304 to 53.962°.
Index ranges	$-14 \leq h \leq 14$, $-34 \leq k \leq 34$, $-21 \leq l \leq 21$
Goodness-of-fit on F^2	1.041
R indices (all data)	R_1 = 0.0707, wR_2 = 0.2038

#Crystallographic data have been submitted to the Cambridge Crystallographic Database with according reference numbers CCDC 2573837.

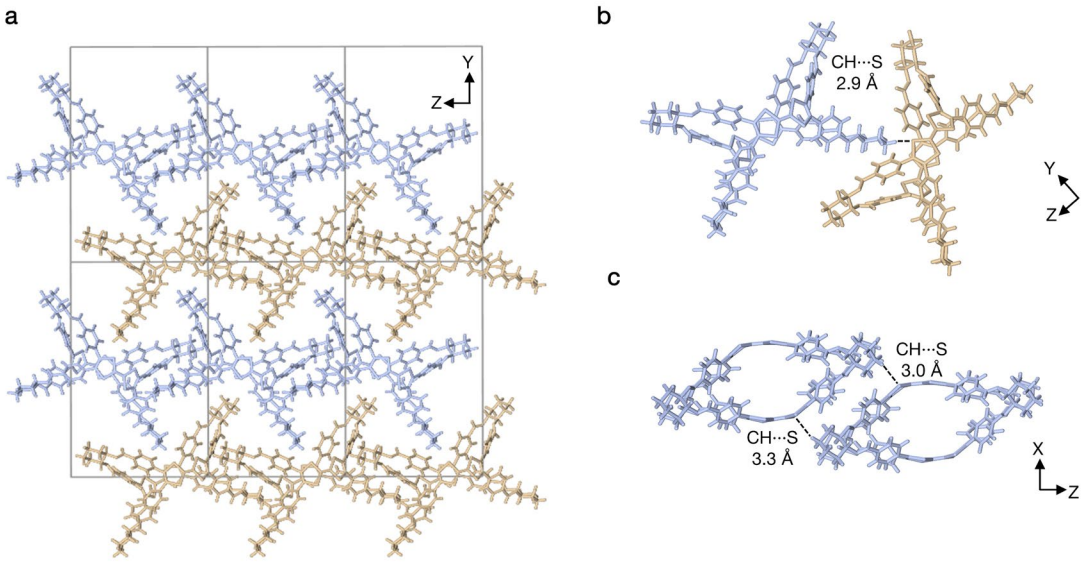

Figure S10. (a) Crystal packing of TTFcage structure viewed along the *yz* plane that shows the arrangement of the adjacent cages. (b) Magnified view of the two adjacent TTFcage in (a) to highlight the CH···S interactions (2.9 Å) that bind the two cages along the *xz* plane. c) Magnified view of the two adjacent TTFcages to highlight another form of CH···S interactions (3.0 Å and 3.3 Å) along the *xz* plane.

Table S2. Crystallographic data of the ReTTFcage obtained from $CHCl_3/CH_3OH$.

Empirical formula	$C_{98}H_{96}F_6N_8S_8$
Formula weight	1756.31
Temperature	193.00 K
Wavelength	Ga Kα (λ = 1.34139 Å)
Crystal system	Tetragonal
Space group	$I4_1/a$
Unit cell dimensions	a = 28.750(3) Å
	b = 28.750(3) Å
	c = 28.176(4) Å
	α = 90°
	β = 90°
	γ = 90°
Volume	23289(5) $Å^3$
Z	8
Density (calculated)	1.002 g/cm^3
Absorption coefficient	1.195 mm^{-1}
F(000)	7408.83
Theta range for data collection	4.304 to 51.498°.
Index ranges	$-33 \leq h \leq 33$, $-33 \leq k \leq 33$, $-32 \leq l \leq 32$
Goodness-of-fit on F^2	1.051
R indices (all data)	R_1 = 0.1416

Crystallographic data have been submitted to the Cambridge Crystallographic Database with according reference numbers CCDC 2565994.

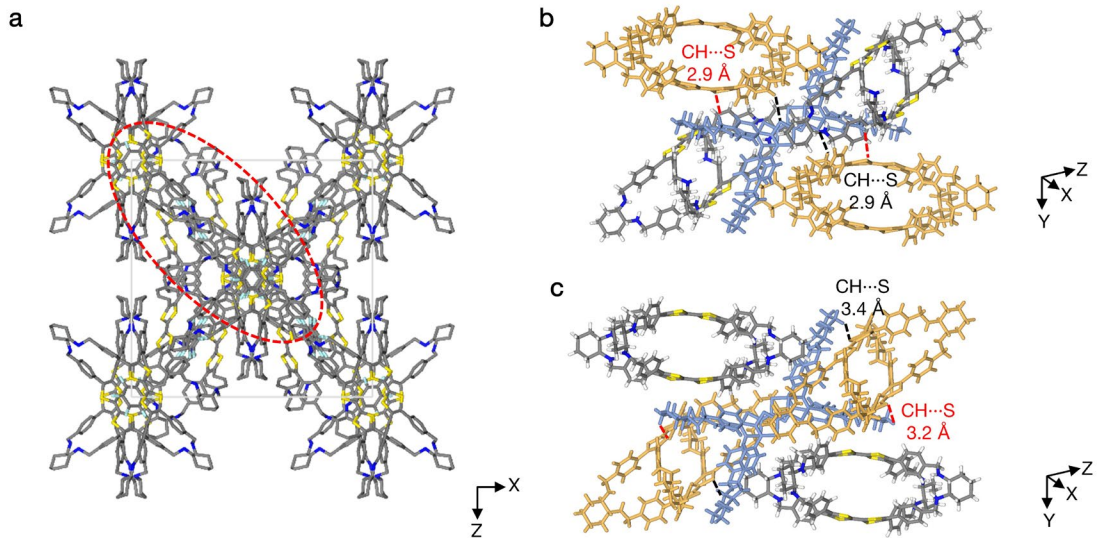

Figure S11. (a) Crystal packing of ReTTFcage structure viewed along the *xz* plane that shows the arrangement of the adjacent cages, where the neighboring cages are packed in an alternating manner, forming a body-centered cubic lattice. (b) Magnified view of the central ReTTFcage (blue color) to highlight its multiple CH···S interactions (2.9 Å) to the two adjacent cages (yellow). (c) Magnified view of the central ReTTFcage (blue color) to highlight the other forms of CH···S interactions (3.2 Å and 3.4 Å) to another two adjacent cages (yellow).

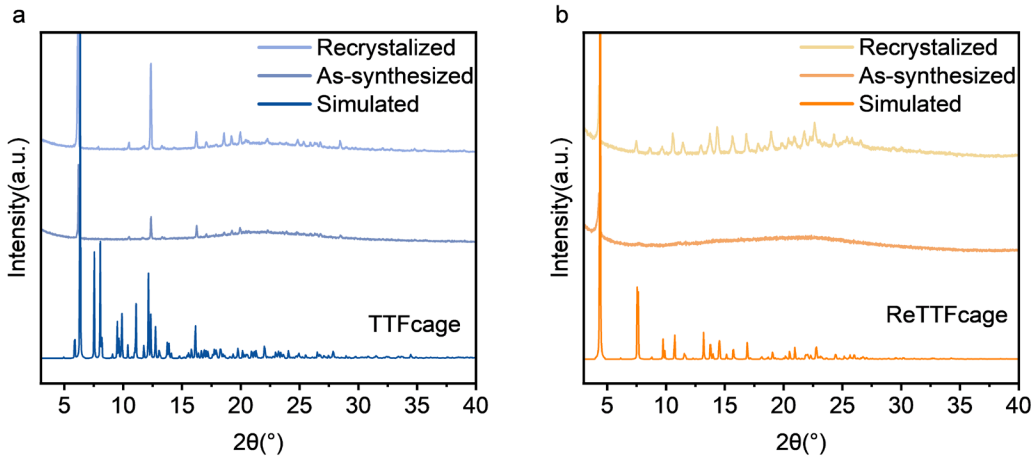

Figure S12. PXRD curve of a) as-synthesized (grey), recrystallized (light blue), and simulated (deep blue) TTFcage, b) as-synthesized (yellow), recrystallized (light orange), and simulated (deep orange) ReTTFcage.

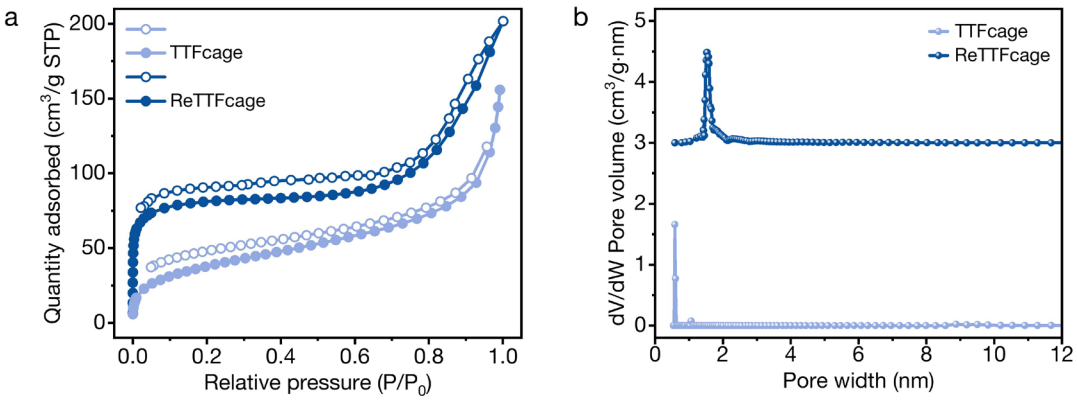

Figure S13. a) N_2 adsorption (solid circles) and desorption (open circles) isotherm of TTFcage (light blue) and ReTTFcage (deep blue) at 77 K. b) Pore size distribution of TTFcage (light blue) and ReTTFcage (deep blue) from NLDFT model.

BET analysis indicates that the surface area of ReTTFcage is determined to be 245 m^2 g^{-1} with a microporous size of 1.5 nm, slightly higher than that of TTFcage parent (169 m^2 g^{-1}, 0.6 nm pore size).

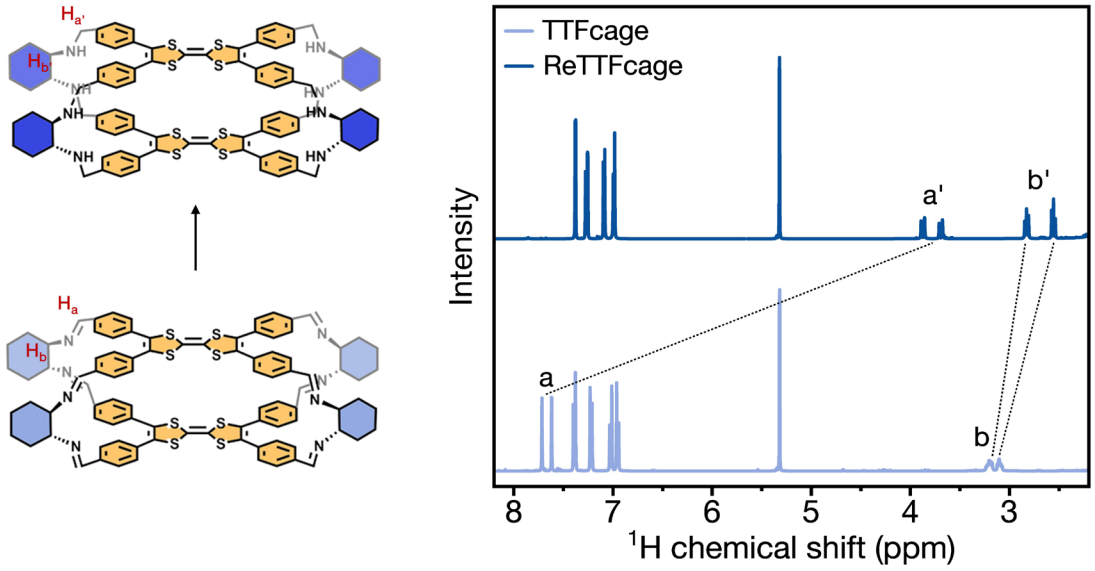

Figure S14. ^{1}H NMR spectra to identify the structural conversion from TTFcage parent to the reduced ReTTFcage.

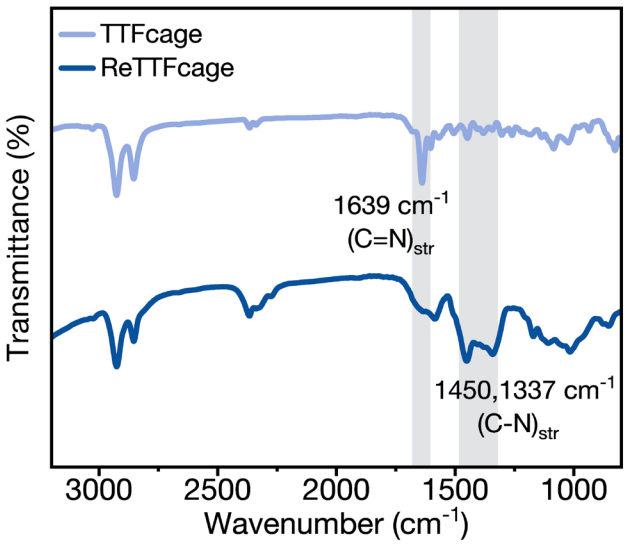

Figure S15. IR spectra to show the structural conversion from TTFcage parent to the reduced ReTTFcage.

3. Static Adsorption Performance of ReTTFcage.

PFOA adsorption experiments. Batch uptake experiments were conducted using the prepared PFOA solution (C_0 = 1000 ng L^{-1}) as adsorbate and ReTTFcage solid powder (2.0 mg) as adsorbent. ReTTFcage solution (1.0 mg mL^{-1}, 2 mL) was added into 50 mL of PFOA solution to form a suspension. The suspension was continuously stirred until aliquots of samples were taken out for further analysis at a given time interval. Samples were collected in 1 mL volume and filtered with a 0.2 μm syringe filter to remove the solid particles, and then subjected to quantitatively analyze by LC-MS. All adsorption experiments were performed in triplicate. In parallel, we also used TTFcage counterpart and activated carbon (AC) as adsorbents to undergo the PFOA adsorption with the same conditions. For the case of other PFAS uptake, the experimental process and operation is identical and the initial PFAS concentration was fixed at 1000 ng L^{-1}.

The removal efficiency (%) of PFOA as a function of time can be expressed as Eq.(2),

$$Removal\ efficiency\ (\%) = \frac{C_0 - C_t}{C_0} \times 100\% \ldots\ldots\ldots\ldots (2)$$

Where C_0 (ng L^{-1}) and C_t (ng L^{-1}) are the initial PFOA concentration and the residual concentration of PFOA at the given adsorption time, t (min), in the filtrate, respectively. From the removal amount, we can obtain that the adsorption capacity of cage materials is determined as Eq.(3),

$$Q_t = \frac{C_0 - C_t}{C_A} \ldots\ldots\ldots\ldots (3)$$

Where Q_t (mg g^{-1}) represents the PFOA uptake adsorption at time t, while C_0 (ng L^{-1}) and C_t (ng L^{-1}) are the same as in Eq.(1), and C_A (mg mL^{-1}) is the concentration of cage adsorbent (ReTTFcage). The data from the adsorption kinetics were fitted against the pseudo-first-order and pseudo-second-order adsorption models in a linear or nonlinear form represented by Eq.(4) and Eq.(5-6), respectively,

$$Pseudo - first\ order\ model\text{: } \ln(Q_e - Q_t) = -k_{1,obs}t + \ln Q_e \ldots\ldots\ldots\ldots (4)$$

$$Linear\ Pseudo - second\ order\ model\text{: } \frac{t}{Q_t} = \frac{t}{Q_e} + \frac{1}{k_{2,obs}Q_e^2} \ldots\ldots\ldots\ldots (5)$$

$$Nonlinear\ Pseudo-second\ order\ model: Q_t = \frac{k_{2,obs} Q_e^2 \cdot t}{k_{2,obs} Q_e \cdot t + 1} \ldots\ldots\ldots\ldots (6)$$

Where t (min) is the time, Q_e (mg g^{-1}) is the amount of PFOA uptake by cage materials at equilibrium, $k_{1,obs}$ and $k_{2,obs}$ are the apparent adsorption rate constants for the pseudo-first-order and pseudo-second-order model, respectively.

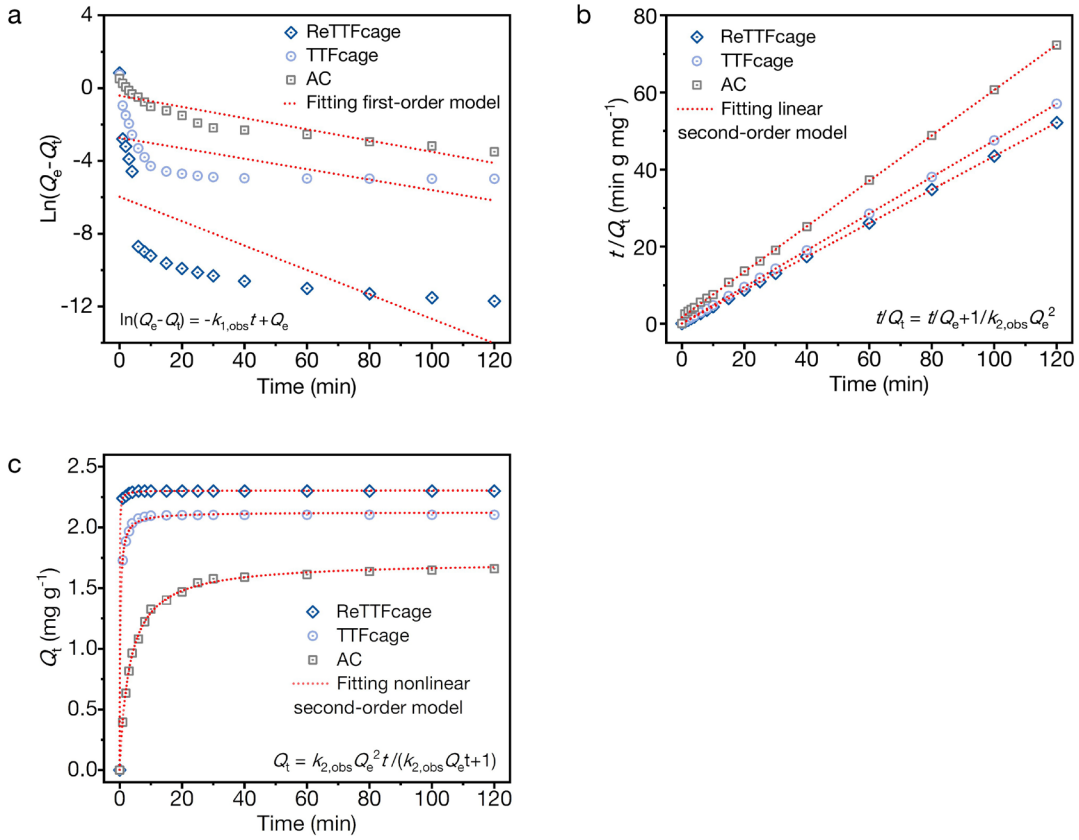

Figure S16. The adsorption kinetic curves of ReTTFcage (deep blue diamonds), TTFcage counterpart (light blue circles), and AC benchmark material (grey squares) and their fitting for diverse models (red dot lines): a) pseudo-first-order model, b) linear pseudo-second-order model, and c) nonlinear pseudo-second-order model.

From the above results and the parameter summary in *Table S2*, it can be seen that the adsorption kinetic data of three adsorbents toward PFOA best fit linear pseudo-second-order curves, exhibiting the correlation coefficient close to 1.0 (R^2, 0.982~0.993), thus the adsorption rate of ReTTFcage is determined to be 60500 g mg^{-1} h^{-1}, far higher than its TTFcage parent (639 g mg^{-1} h^{-1}) and AC benchmark material (20.7 g mg^{-1} h^{-1}).

Table S3. Adsorption kinetic parameters of three adsorbents fitting for different kinetic models.

Adsorbents	**Pseudo-first-order model**		**Linear pseudo-second-order model**		**Nonlinear pseudo-second-order model**	
	$k_{1,obs}$ (g mg^{-1} h^{-1})	R^2	$k_{2,obs}$ (g mg^{-1} h^{-1})	R^2	$k_{2,obs}$ (g mg^{-1} h^{-1})	R^2
ReTTFcage	4030	0.401	60500	0.993	63560	0.985
TTFcage	1730	0.329	639.0	0.991	286.4	0.973
AC	1850	0.811	20.7	0.982	12.8	0.977

Table S4. Summary of the maximum adsorption capacity (Q_m) and adsorption kinetics (k_{obs}) of PFOA by ReTTFcage and other benchmark porous materials.

[a]Category	Adsorbent Name	Q_m (mg g^{-1})	k_{obs} (mg g^{-1} h^{-1})	Equilibrium (min or h)	Initial PFOA (ng L^{-1})	Ref.
[b]MOF	UiO66-F4-OS	3631.3	0.173	24 h	100000	9
	PCN-224	963	0.33	1 h	1000	10
	MIL-101	44.3	0.077	1.5 h	1000	11
	PCN-999	1089	1.38×10^{-3}	12 h	1000	12
	PCN-1002	632	3.07×10^{-3}	15 min	1000	13
	MOF-DUT67	383	n/a	n/a	2000	14
	Fe-BTC	548	0.0979	2 h	n/a	15
	Fe-MIL-100	427	0.609	2 h	n/a	15
	Fe-MIL-101	490	0.168	2 h	n/a	15
	In(tcpp)	980	4.82	12 h	100	16
COF	Cys-COF	530	0.0751	1 min	1000	17
	COF-SP	631	29.2	0.5 min	1000	18
	TG-PD COF	2600	152100	30 min	1000	19
	MELEM COF	2500	1263	30 min	200	20
	COF-I	19.3	943	25 min	n/a	21
	VZ-COF	1000	807	10 min	1000	22
	COF-300	259	n/a	18 h	n/a	23
	QA-F-COF	630	0.0498	0.5 min	1000	18
NAC	F-Cage2	45	441000	2 min	1500	24
	Zn-Cage	1420	n/a	1 h	1500	25
MOC	4b	1223	1.52×10^{-4}	12 h	1000	26
	F-ZrMOC	n/a	n/a	2 h	1000	27
POC	p-A2B3	n/a	n/a	n/a	1000	28
	b-CDcage	23	3189	20 min	1500	29
POP	PAF-1-NDMP	1320	5749	20 min	1000	30
	PAF-1-NDMB	2000	21166	20 min	1000	30
	PAF-1-NDMH	960	14362	20 min	1000	30
	DFB-CDP	64.8	62.5	1 h	1000	31
Hydrogel	3D-PSHΔ	51.2	1.2338	10 h	500	32
	3D-SHΔ	33.6	8.57×10^{-3}	10 h	500	32

	QFgels	2150	4.4×10^{-4}	30 min	1000	33
[c]Industry	AC-PAC	302	20.8	15 h	1000	34
	AC-GAC	178	4.7	15 h	1000	34
	commercial AC	198	20.7	1 h	1000	35
this work	**TTFcage**	**2920**	**639**	**10 min**	**1000**	
	ReTTFcage	**4210**	**60500**	**5 min**	**1000**	

[a]The data of maximum adsorption capacity and adsorption kinetics are obtained at room temperature and a certain PFOA initial concentration in water. [b]MOF = metal-organic framework, COF = covalent organic framework, NAC = nonporous adaptive crystal, MOC = metal-organic cage, POC = porous organic cage, POP = porous organic polymer, Hydrogel = polymer hydrogels, Industry = activated carbons (AC). [c]The commercially available AC is used as the benchmark PFOA adsorption material.

PFOA isotherm adsorption studies. Adsorption isotherm experiments were performed in 20 mL glass vials with stirring (800 rpm) on a heating plate to keep temperature at 25 °C. ReTTFcage powder sample (10 mg) was used for all the tests and varying concentrations of PFOA aqueous solutions with increments at 0.2, 2, 20, 200, 400, 800, 1000, 2000, 3000, and 5000 mg L^{-1} (10 mL) were added to the vials and ultrasonicated for 5 min to form suspensions. Each suspension was stirred for 24 h to reach the equilibrium, subsequently, 1 mL of sample was taken out and filtered by 0.2 μm syringe filters to remove the remaining adsorbent. The filtrate was analyzed through LC-MS. All the isotherm adsorption experiments were conducted in triplicate. As control, we also used TTFcage counterpart and activated carbon (AC) as adsorbents to proceed the isotherm adsorption experiments in the same way. The data were fitted to Langmuir and Freundlich isothermal models, as Eq.(7) and Eq.(8),[35]

$$Langmuir\ model\text{:}\ \frac{C_e}{Q_e} = \frac{C_e}{Q_m} + \frac{1}{Q_m K_L} \ldots\ldots\ldots\ldots (7)$$

Where Q_m (mg g^{-1}) is the maximum adsorption capacity of the adsorbent, C_e (mg L^{-1}) represents the residual PFOA concentration at the equilibrium state. K_L (L mg^{-1}) is the Langmuir adsorption-affinity constant.

$$Freundlich\ model\text{:}\ Q_e = K_F C_e^{1/n} \ldots\ldots\ldots\ldots (8)$$

where K_F is a Freundlich empirical constant, reflecting the relative adsorption capacity, and n is the heterogeneity factor, reflecting the non-uniformity of the adsorption process.

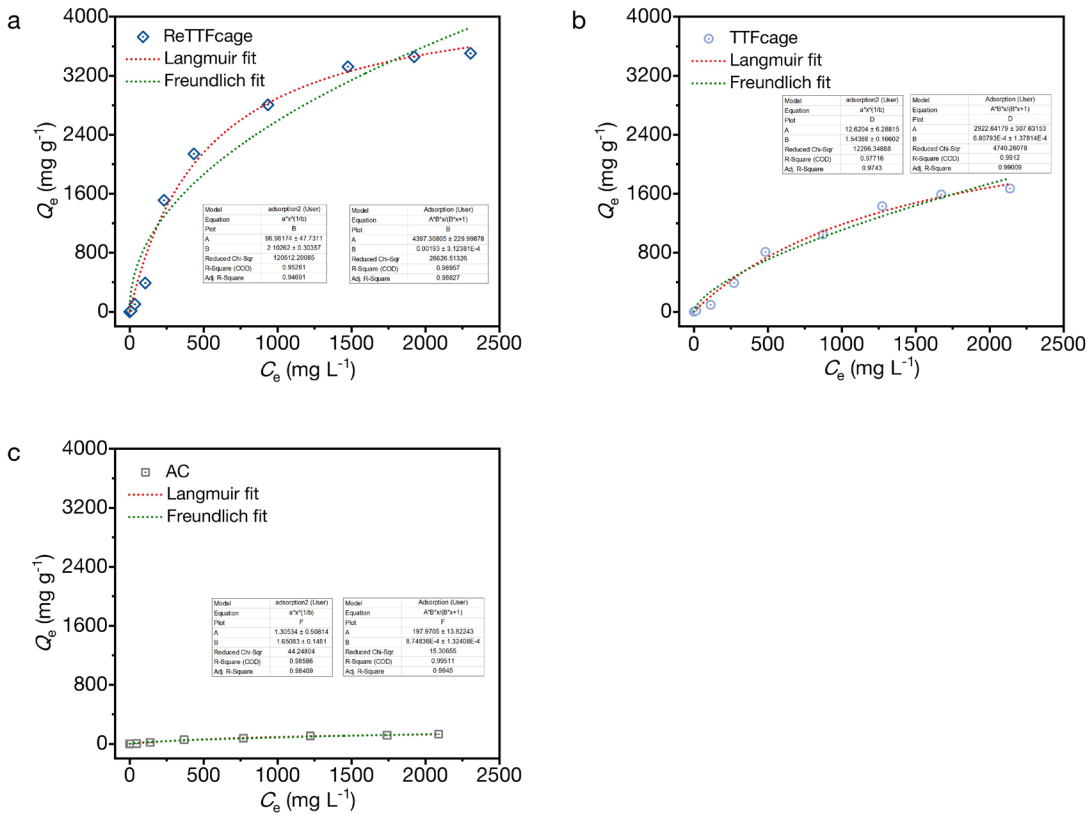

Figure S17. Isotherm adsorption of PFOA by various adsorbents: a) ReTTFcage, b) TTFcage counterpart, and c) AC benchmark material. The curves fitting for Langmuir model (red dot line) and Freundlich model (green dot line).

From the above fitting data and the parameter summary of *Table S4*, it is found that the maximum adsorption capacity of three adsorbents toward PFOA best fit the Langmuir model with higher correlation coefficient ($R^2 > 0.988$). Thus, the adsorption capacity of ReTTFcage is determined to be 4210 mg g^{-1}, ~1.5 times higher than that of TTFcage parent (2920 mg g^{-1}) and 21 times higher than that of commercial AC material (198 mg g^{-1}).

Table S5. Isotherm adsorption parameters of three adsorbents fitting for two adsorption models.

Adsorbent	Langmuir model			Freundlich model		
	Q_m (mg g^{-1})	K_L (L mg^{-1})	R^2	K_F (mg $g^{-1})^{1/n}$	n	R^2
ReTTFcage	4210	1.93×10^{-3}	0.988	96.9	2.12	0.947
TTFcage	2920	6.81×10^{-4}	0.990	12.6	1.54	0.974
AC	198	8.75×10^{-4}	0.995	1.3	1.65	0.984

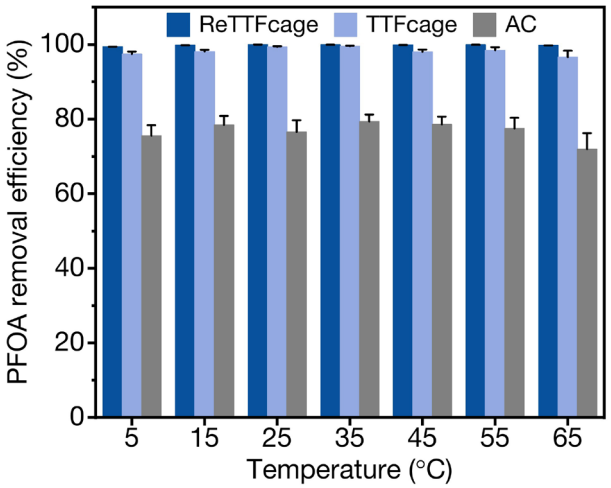

Figure S18. Removal efficiency of PFOA by three adsorbents, ReTTFcage (deep blue columns), TTFcage counterpart (light blue columns), and AC benchmark material (grey columns) at different temperatures (5~65 °C). Initial PFOA concentration is at 1000 ng L^{-1} and three adsorbents are 2 mg. All the error bars represent the standard deviation (*n* = 3 independent experiments).

4. Dynamic Adsorption Performance of ReTTFcage.

Dynamic breakthrough experiments. The continuous-flowing adsorption experiments were conducted on a fixed bed column at ambient temperature, and three adsorbents (20 mg), including ReTTFcage, TTFcage counterpart and AC, were used as the column materials. The feedstock stream was prepared by spiking the water with different concentrations of PFOA (100 μg L^{-1}, 10 μg L^{-1}, 1000 ng L^{-1}, 100 ng L^{-1}, 10 ng L^{-1}, and 1 ng L^{-1}). First, we surveyed dynamic breakthrough adsorption for high concentration of PFOA (100 μg L^{-1}). The PFOA-spiked aqueous solution was pumped through the column by a peristaltic pump at a flow rate of 50 mL min^{-1}, and the column effluents were collected in 1.0 mL aliquots, which was in-line assessed by LC-MS method or the fabricated cage-based field-effect transistor sensor (cageFET). Second, we also tuned the flow rate from 50 mL min^{-1} to 1000 mL min^{-1} and recorded their dynamic uptake performance for emulating the real scenes of environmental water bodies. The absolute in-solution adsorption amount (Q_s) of PFOA species can be calculated as Eq.(9),

$$Q_s(t) = \frac{V_t^{in} \cdot t - V_{dead} - \int_0^t V_t^{out} dt}{m_0} \quad \ldots\ldots\ldots\ldots (9)$$

Where V_t^{in} is the volume influent flow rate of PFOA-spiked solution and V_t^{out} is the solution effluent flow rate, t is the adsorption time, m_0 is the initial mass of the cage adsorbent in solution, and V_{dead} is the dead volume of the system.

Table S6. Dynamic adsorption performance of PFOA among three adsorbents.

pollutant	ReTTFcage		TTFcage		AC	
	Initial[a] ($ng\ L^{-1}$)	Residue[b] ($ng\ L^{-1}$)	Initial ($ng\ L^{-1}$)	Residue ($ng\ L^{-1}$)	Initial ($ng\ L^{-1}$)	Residue ($ng\ L^{-1}$)
PFOA	1000	0.082	1000	1.39	1000	92.53
	100000	2.73	100000	36.31	100000	7825.5

[a]The initial PFOA is at a given concentration (1000 ng L^{-1} or 100000 ng L^{-1}).

[b]After dynamic breakthrough adsorption by different adsorbents, the residual PFOA concentration in the filtrates.

Table S7. Comparison of dynamic adsorption performance for PFOA by ReTTFcage and typical porous materials.

Category	Adsorbent	BV[a] (mL)	Flow rate (mL min^{-1})	Adsorbent amount (mg)	Initial PFOA conc.[b] (ng L^{-1})	Residual PFOA conc. (ng L^{-1})	Ref.
COF	TG-PD COF	20	0.1	3.0	1000	<50	19
		20	0.1	3.0	2×10^5	<50	19
NAC	F-Cage2	10	0.67	20	1500	6	24
MOC	4b	5	60	30	1×10^8	<5	26
	F-ZrMOC	40	n/a	20	8000	1.44	27
POP	PAF-1-NDMB	3530	n/a	300	5×10^5	53	30
		9.5	n/a	1000	4×10^8	31	30
Hydrogel	QFgels	2000	1388	1.18×10^7	350	80	33
Industry	AC	327	50	20	1000	92.53	35
This work	**TTFcage**	**3080**	**50**	**20**	**1000**	**1.39**	
	ReTTFcage	**1480**	**50**	**20**	**1000**	**0.082**	
	TTFcage	**1610**	**1000**	**20**	**1000**	**16.25**	
	ReTTFcage	**2470**	**1000**	**20**	**1000**	**0.67**	

[a]BV represents the breakthrough volume in dynamic adsorption experiments.

[b]The initial PFOA concentration and residual PFOA concentration can be assessed the dynamic adsorption capacity of diverse adsorbents.

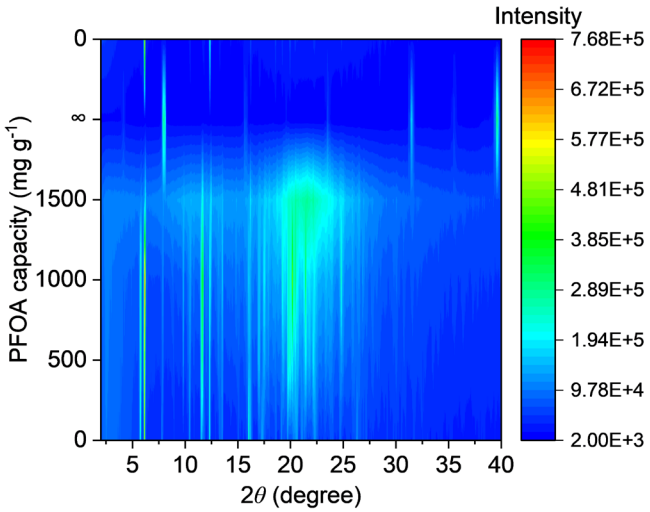

Figure S19. The PXRD results show the adsorption of PFOA by ReTTFcage powder and the regeneration process. From bottom to top, they are the initial ReTTFcage, PFOA@ReTTFcage after adsorbing a certain amount of PFOA, PFOA, and the regenerated ReTTFcage after methanol washing to remove the guest. It can be seen that the crystallinity of ReTTFcage is not damaged after adsorbing PFOA. After methanol washing, some diffraction peaks of ReTTFcage still remain, indicating that the material has been successfully regenerated and can be recycled.

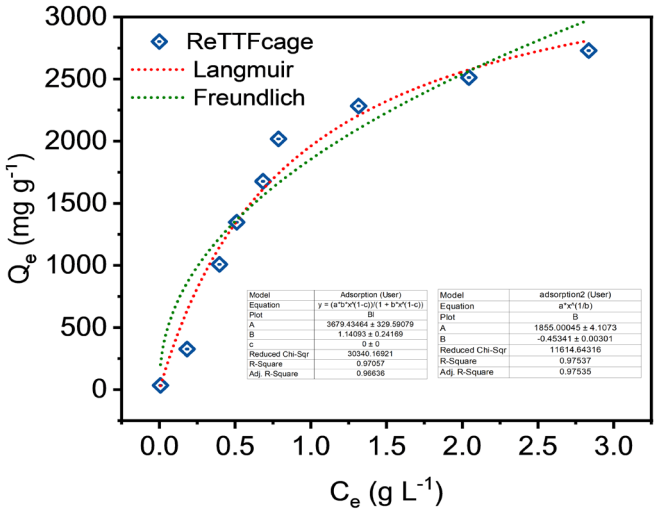

Figure S20. Isotherm adsorption model fitting of PFOA elution solution.

Specifically, ReTTFcage containing PFOA was washed with clean water and dried, and then ultrasonically eluted in a methanol/sodium chloride solution for the quantitative detection of PFOA. Based on the comparison of fitting parameters, the maximum adsorption capacity of ReTTFcage for PFOA is 3679 mg g^{-1} ($R^2 > 0.971$).

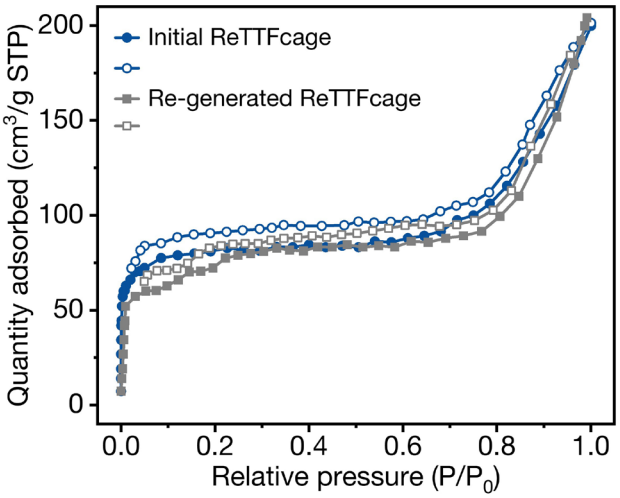

Figure S21. BET surface area analysis for showing the regeneration of guest-free ReTTFcage: initial ReTTFcage (blue line) and re-generated ReTTFcage without guest through methanol washing (grey line).

It can be seen that after washing the re-formed cage material has the similar specific surface area, indicating the cage regeneration with the recovery of pore structure and porosity.

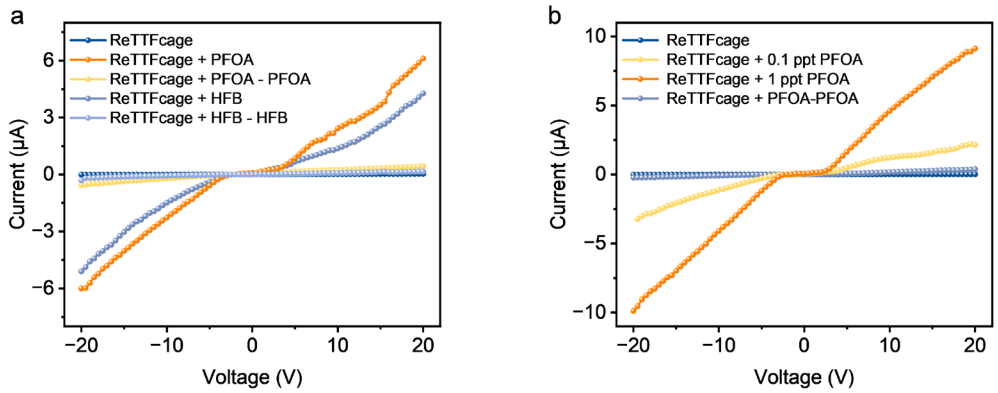

Figure S22. Current-voltage (I-V) curves show the conductivity of ReTTFcage with a) different guest molecules and b) different concentrations of guest molecules.

It can be seen that ReTTFcage without guest molecules has extremely low conductivity, while as the fluorine-containing guest molecules are introduced, the conductivity will significantly increase. Interestingly, after the guest molecules are removed, the conductivity of ReTTFcage will return to its original level.

5. Field-Effect Transistor Sensor Fabricated by ReTTFcage.

Fabrication of cage-based field-effect transistor (cageFET). A silicon wafer with 300 nm of SiO_2 layer (Guangzhou Fangdao Semiconductor Inc.) was used as the substrate. Source and drain electrode were defined by S1813 photoresist using photolithography technology (MicroWrite ML3 laser direct writing photoengraving machine, Durham Magneto Optics Ltd.). ReTTFcage solution (0.1 mg mL^{-1}, $CHCl_3/CH_3OH$, v/v, 3/1) was drop-casted on the surface of SiO_2 layer to form 50 nm of thin film channel material that connected with the upper drain and source to fabricate a bottom-gate top-contact FET configuration. Then, 25 nm of Au layer with Cr were thermally evaporated and patterned by stripping the photoresist layer (stripper: Remover PG, MicroChem). The wafer with electrodes was processed with a hydrophobic treatment. O_2 plasma (100 W, 0.4 sccm) was applied to the wafer. In a vacuum oven, octadecyltrichlorosilane (OTS, Maklin Inc.) was deposited at a temperature of 120 °C for 75 min, thus fabricating a self-assembled monolayer. The obtained device was sonicated in heptane to remove the redundant OTS molecules and dried for use. An Ag/AgCl electrode was set to exert the gate voltage (V_{gs}) through the analyte solution in a polydimethylsiloxne (PDMS) well. The whole cageFET device was fabricated into the size of 1 × 1 cm.

CageFET Device Measurement. The electrical measurement was conducted on 2612B semiconductor analyzer of Keysight (Santa Clara, California, USA). For measurement of I_{ds}–V_{gs} curve, a gate voltage ranging from 10 V to -20 V was applied to the Ag/AgCl reference electrode acting as the liquid gate electrode. For measurement of the current response, the V_{gs} was set at -12 V for observing the I_{ds} change with analyte concentration. The analyte solution (PFOA solution with a given concentration) was in the PDMS well for measurement. The carrier mobility of this cageFET device was extracted from the transfer curves by the formula of Eq.(10),

$$I_{ds} = W \cdot \mu \cdot C \cdot \frac{(V_{gs} - V_{th})^2}{2L} \quad \ldots\ldots\ldots\ldots (10)$$

where W and L are the width and length of the gate channels (1000 μm and 50 μm), μ

is carrier mobility and C is specific capacity of dielectric layer (11 nF cm^{-2} for SiO_2 layer). By fitting the linear region of the curves of $I_{ds}^{1/2}$ versus V_{gs}, μ was obtained.

Sensing mechanism of CageFET with analyte concentration. As is given by Nernst equation, the response of FET sensor can be expressed as the following Eq.(11),

$$V_{channel} = V_0 + \frac{RT}{nF} \ln C_{analyte} \ldots\ldots\ldots\ldots (11)$$

where $V_{channel}$ is the potential of channel; V_0 is the initial potential; $C_{analyte}$ represents the concentration of analyte, PFOA in this case; R is the gas constant and F is the Faraday's constant. T represents the temperature.

In a cageFET sensor, the relationship between drain-source voltage (V_{ds}), gate-source voltage (V_{gs}) and drain-source current (I_{ds}) can be described as Eq.(12),

$$I_{ds} = \frac{\mu W}{L} C_{gate} V_{ds} \left(V_{gs} - V_{channel}\right) \ldots\ldots\ldots\ldots (12)$$

Where μ is the carrier mobility; W and L represent width and length of the channel, respectively, while C_{gate} is the capacitance of the ReTTFcage. Combining Eq.(11) and Eq.(12), it can be calculated the I_{ds} and $C_{analyte}$ that follow the relationship as Eq.(13),

$$I_{ds} = \frac{\mu W}{L} C_{gate} V_{ds} \left(V_{gs} - V_0 - \frac{RT}{nF} \ln C_{analyte}\right) \ldots\ldots\ldots\ldots (13)$$

Where the physical quantities (W, L, R, T, and F) are constants and other parameters remains unchanged. Accordingly, from the above equation, it is clear that I_{ds} is linearly correlated with the concentration of PFOA, following the relationship as below,

$$I_{ds} = a \cdot \ln C_{PFOA} + b$$

Here, a and b are regarded as the constants and hence ΔI_{ds} would be linearly depended on the logarithm of C_{PFOA}.

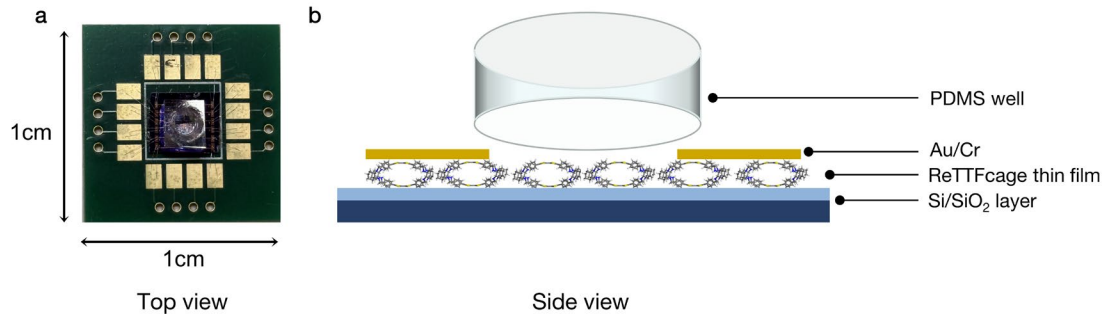

Figure S23. The cageFET device structure: (a) top view showing the practical device photograph, (b) side view showing the device compositions. The ReTTFcage thin-film was contacted between the Si/SiO_2 layer and Au electrodes. ReTTFcage film was used as the conductive channel and sensing material.

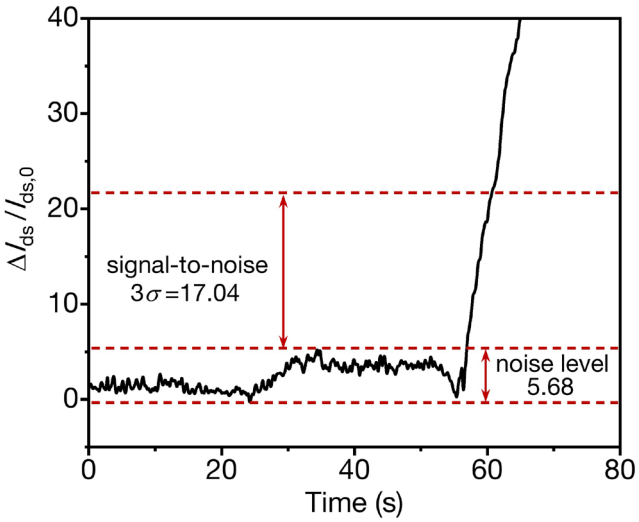

Figure S24. LoD calculation from the signal-to-noise ratio in current response. In the absence of PFOA species, the normal $\Delta I_{ds}/I_{ds,0}$ response background as a function time shows the noise perturbation of 5.68. Hence, the 3σ value (signal-to-noise) is 17.04. With this value and the quantitative relationship between $\Delta I_{ds}/I_{ds,0}$ and PFOA content ($\Delta I_{ds}/I_{ds,0} = 34.325\log C_{PFOA} + 436.068$), the LoD is calculated to be 6.2×10^{-13} g L^{-1} (~0.6 ppq).

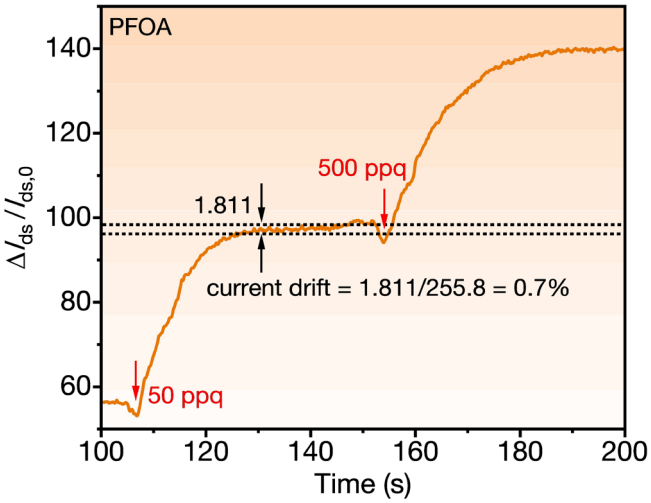

Figure S25. Time-resolved $\Delta I_{ds}/I_{ds,0}$ response of cageFET upon consecutive addition of different concentrations of PFOA from 5 ppq to 5 ppb. Typically, the black arrow represents the current drift percentage after 50 ppq of PFOA (current drift value/total current response = 1.811/255.8 = 0.7%).

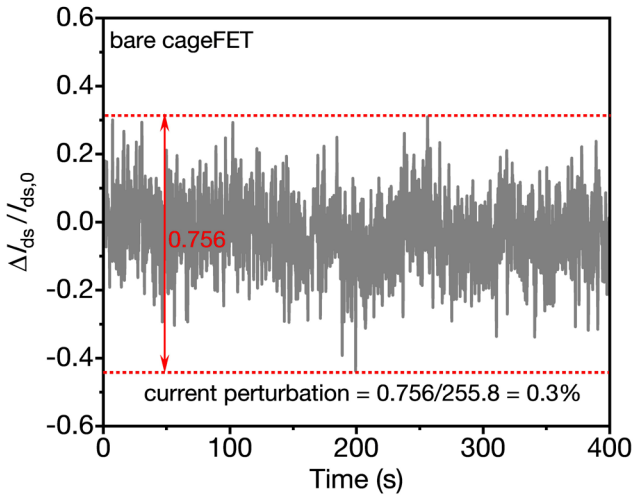

Figure S26. Time-resolved monitoring of bare cageFET in the absence of PFOA to show the stability of device. The maximum perturbation of current response, $\Delta I_{ds}/I_{ds,0}$, is 0.756 within 400 s, which only accounts for 0.3% of total current response.

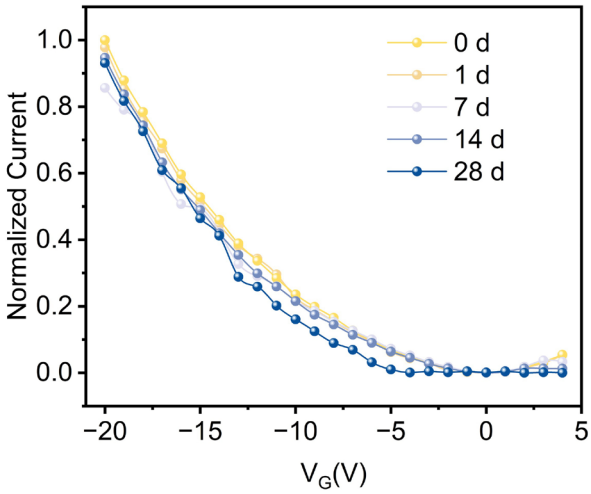

Figure S27. Normalized current response changes of cageFET to PFOA during 28 days. The long-term response tracking results show that the cageFET has a fluctuation of no more than 1.27% in the current response value to PFOA within 28 days.

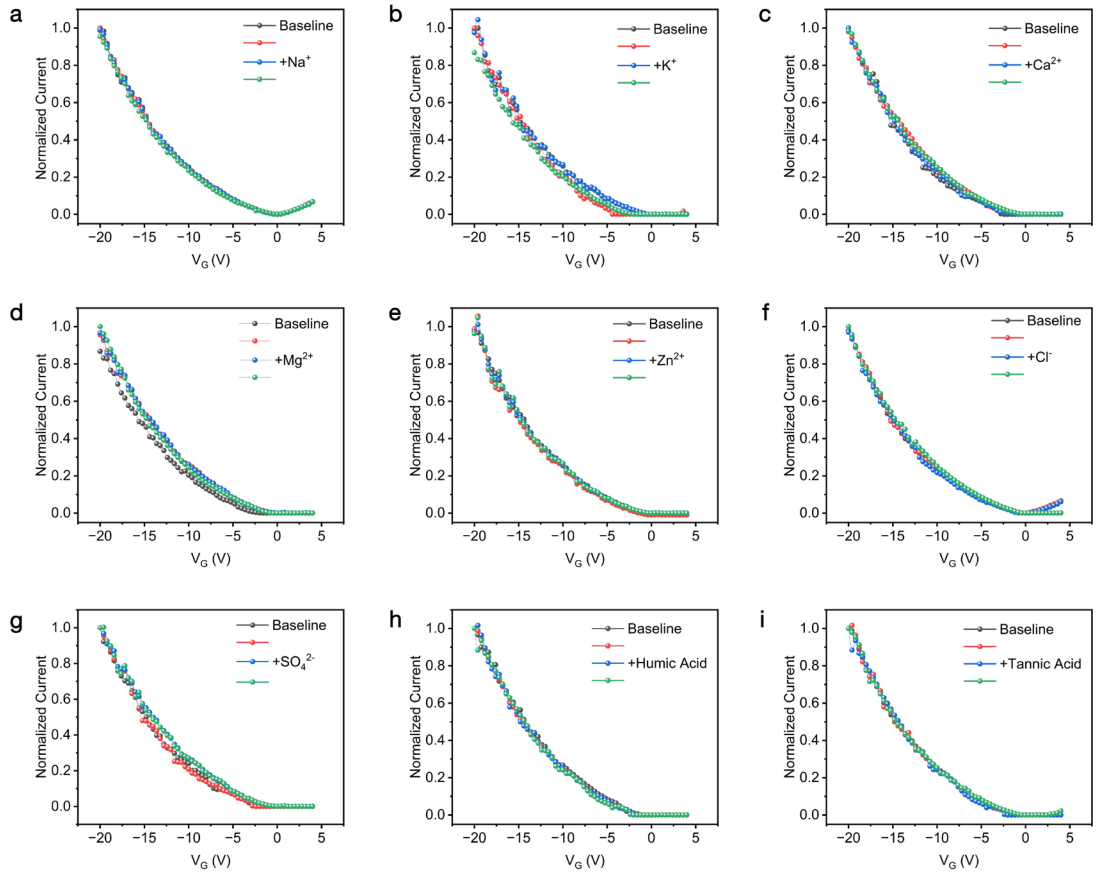

Figure S28. Normalized current response of cageFET in the presence of various cations (Na^+, K^+, Ca^{2+}, Mg^{2+}, and Zn^{2+}), anions (Cl^- and SO_4^{2-}), and dissolved organic acids (HA and TA). Under these diverse interfering species, the response values of cageFET to PFOA showed no significant change.

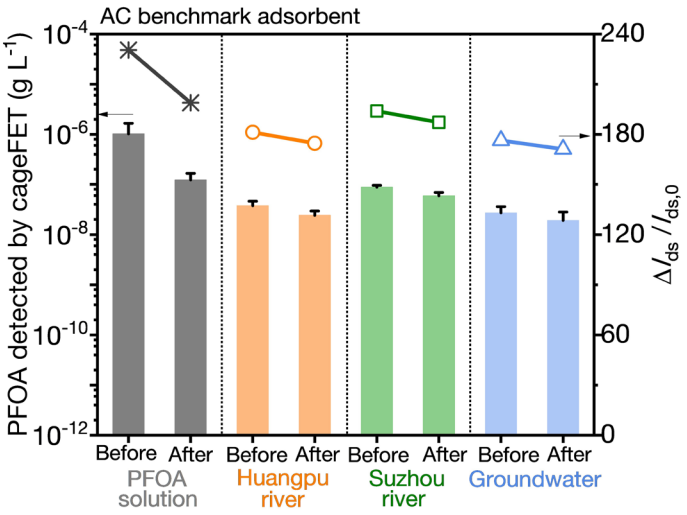

Figure S29. $\Delta I_{ds}/I_{ds,0}$ responses (right y-axis) monitored by cageFET and corresponding PFOA contents of different water samples before and after adsorption (left y-axis) by commercial AC benchmark adsorbent. The real water samples were taken from PFOA-spiked solution (1000 ng L^{-1}), Huangpu River, Suzhou River, and groundwater in Shanghai.

Through cageFET monitoring, it can be seen that the initial PFOA concentration taken from different water samples were determined to be 1012.35 ng L^{-1} (PFOA-spiked solution), 37.63 ng L^{-1} (Huangpu River), 88.23 ng L^{-1} (Suzhou River), and 27.17 ng L^{-1} (groundwater), which are consistent well with the LC-MS results. After adsorption by AC benchmark adsorbent, the PFOA residues were respectively calculated to be 123.77 ng L^{-1} (PFOA-spiked solution), 24.23 ng L^{-1} (Huangpu River), 59.55 ng L^{-1} (Suzhou River), and 19.14 ng L^{-1} (groundwater), which do not match the threshold of U.S.EPA (<4 ng L^{-1}). These results mean that cageFET sensor also demonstrate that the dynamic adsorption ability of AC adsorbent is not suitable for removal of PFOA in real water bodies.

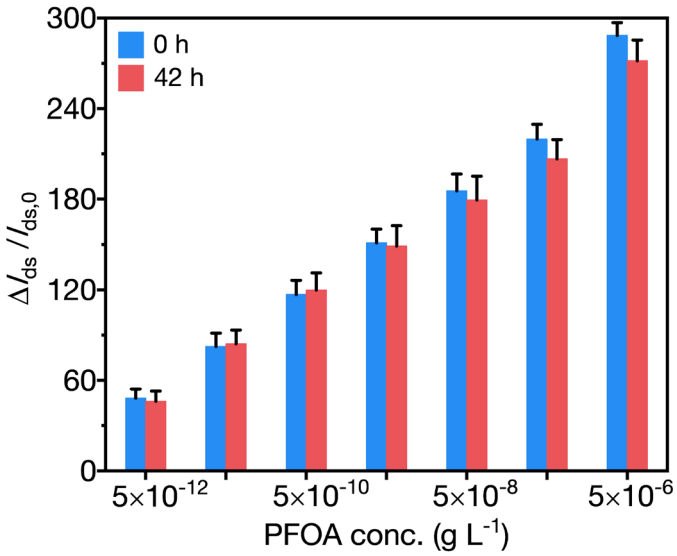

Figure S30. The long-term stability tests of cageFET sensor for 42 h at different PFOA concentrations (5×10^{-12} g L^{-1}, 5×10-^{10} g L^{-1}, 5×10^{-8} g L^{-1}, and 5×10^{-6} g L^{-1}) to show the durability of cageFET device.

Table S8. Performance comparison of diverse sensing and detecting methods for PFOA.

Detecting Methods	Materials Category[e]	Structural Name	LoD (ng L^{-1})	Response time (min)	Instrument size (m)	Ref.
FS[a]	NPs	gMIP@oSNP	45540	~15	0.4	36
	polymers	PPE-Py	100	n/a	0.5	37
	polymers	PT32	17200	2	0.4	38
	MOF	U-1MOF	1280	5	0.6	39
	MOF	In(tcpp)	19000	2	0.5	16
	NAC	Zn-Cage	57	2	0.5	25
	COF	TG-PD	1800	2	0.45	19
	COF	F-MOF	331	5	0.5	40
UV-Vis[b]	MOF	F-Ce-UiO66-NH_2	170000	0.16	0.2	41
	MOF	MGO@ZIF-8	4968	50	0.5	42
EC[c]	MOF	F-Cu-NH2BDC	1.47	n/a	0.37	43
	MOF	Cu-HHTP	0.002	1	0.1	44
	MOF	Ce-UiO66-F	19.8	n/a	0.2	45
LC-MS[d]	-	-	0.2	10	~1	46
This work	**POC**	**ReTTFcage**	**0.0006**	**0.5**	**0.01**	

[a]FS represents fluorescent detecting assay by fluorescent spectroscopy. [b]UV-Vis means colorimetric detecting assay by UV-Vis spectroscopy. [c]EC represents electrochemical sensing or monitoring method by small electrochemical sensor or instrument. [d]LC-MS represents the gold standard in industry. [e]NPs = nanoparticles, polymers = conjugated polymers, MOF = metal-organic framework, COF = covalent organic framework, NAC = nonporous adaptive crystal, POC = porous organic cage.

6. Mechanistic Insight on PFOA Binding by ReTTFcage.

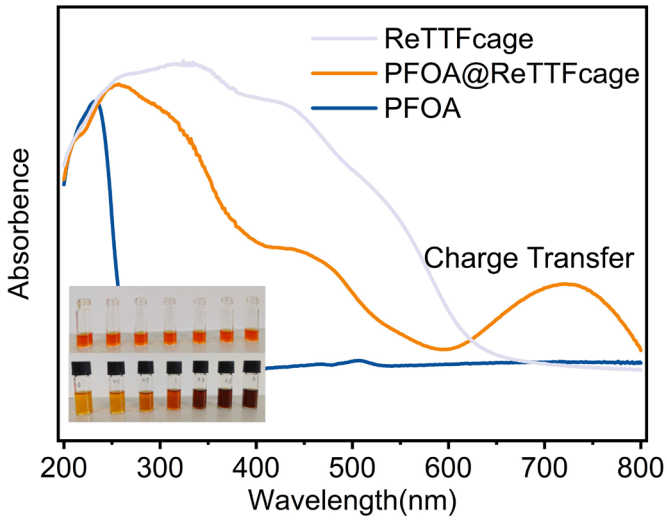

Figure S31. UV-Vis diffuse reflectance spectroscopy of PFOA, PFOA@ReTTFcage, and ReTTFcage.

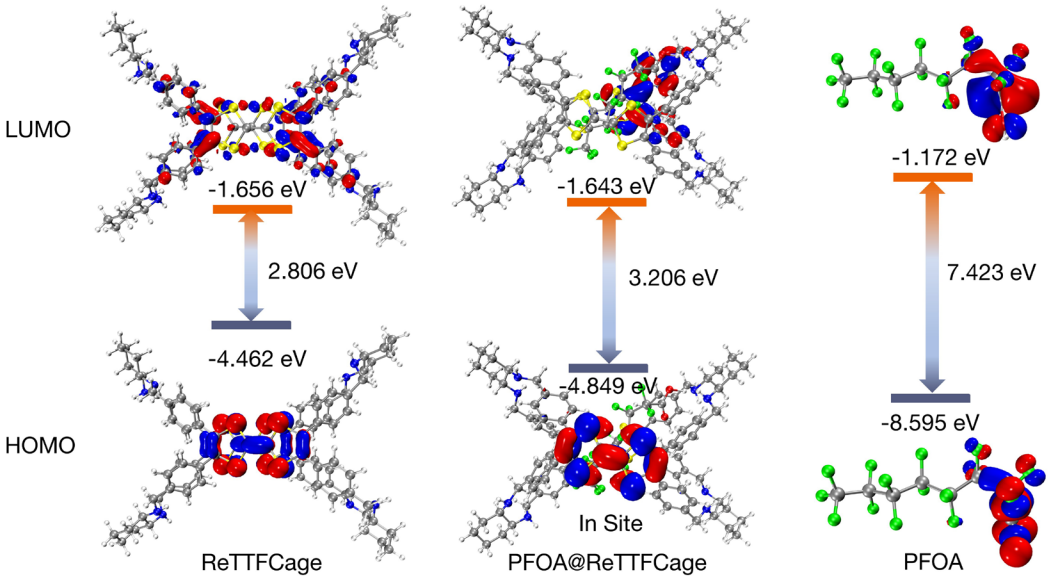

Figure S32. Energy level diagrams of ReTTFcage, PFOA@ReTTFcage, and PFOA by DFT.

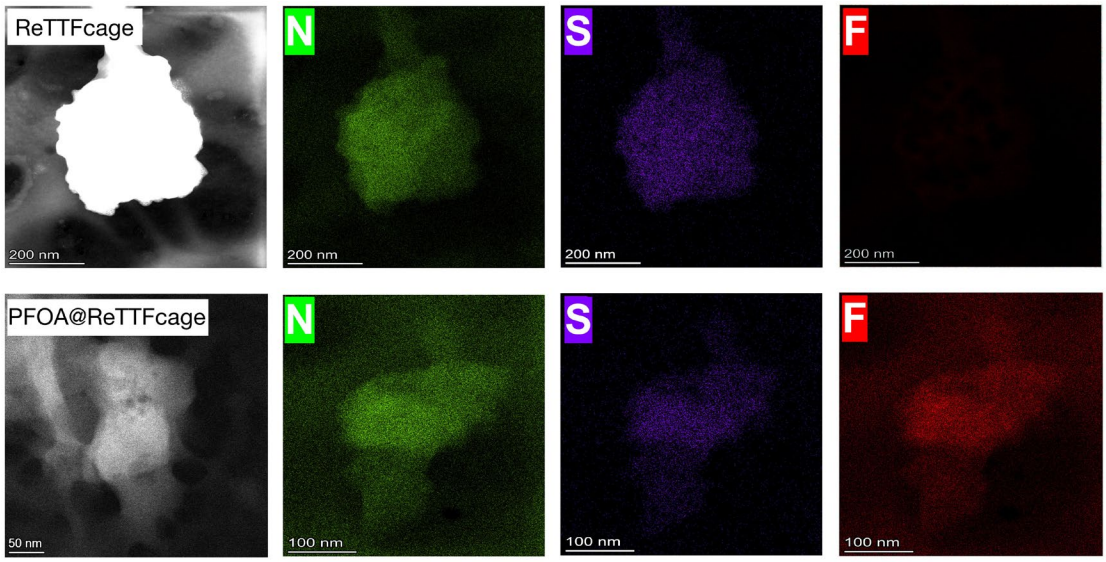

Figure S33. SEM images and EDS mapping of pristine ReTTFcage (top panel) and PFOA@ReTTFcage (bottom panel).

It was found that pristine ReTTFcage had uniform distribution of N and S elements throughout its crystalline microparticles, but without F element. However, after PFOA treatment, in addition to N and S, F element was also uniformly distributed within the particles, which indicates that PFOA species are tightly bound by ReTTFcage.

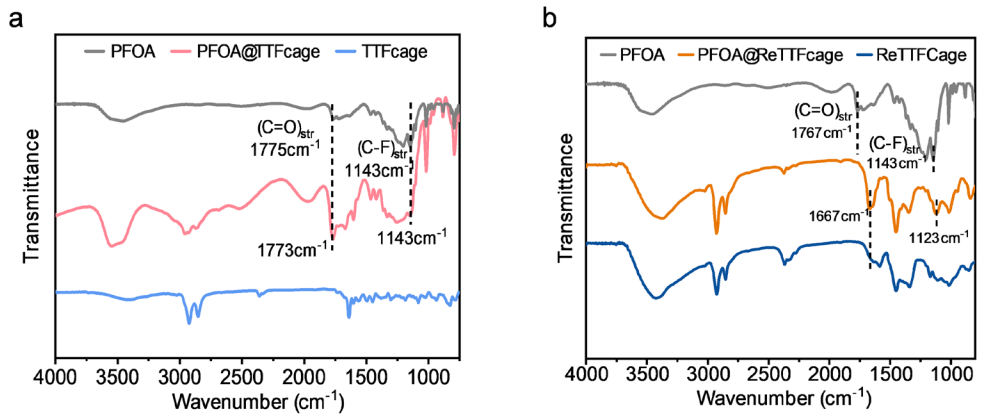

Figure S34. a) FT-IR spectra of PFOA (grey line), pristine TTFcage (blue line), and PFOA@TTFcage (red line). b) FT-IR spectra of PFOA (grey line), pristine ReTTFcage (deep blue line), and PFOA@ReTTFcage (orange line).

From the infrared spectrum, it can be seen that after PFOA adsorption, the corresponding substance of TTFcage shows almost no change compared to PFOA itself. The characteristic C=O stretching vibration (1775 → 1773 cm^{-1}) and C-F stretching vibration (1143 cm^{-1}) did not show any significant changes. In contrast, C=O stretching vibration (1767cm^{-1} → 1667cm^{-1}) and C-F stretching vibration (1143cm^{-1} → 1123cm^{-1}) of PFOA@ReTTFcage shifted significantly. These results indicate that there is a hydrogen bond interaction between ReTTFcage and the carboxyl group end of PFOA, while TTFcage does not.

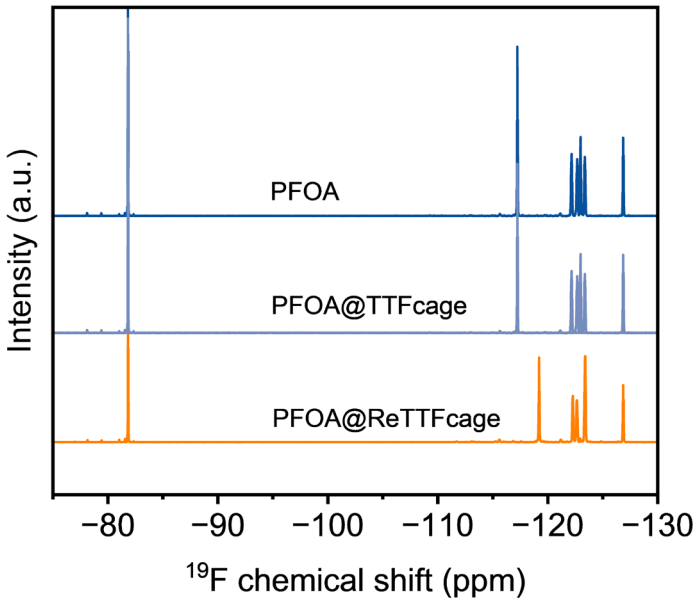

Figure S35. ^{19}F NMR spectra of PFOA, PFOA@TTFcage and PFOA@ReTTFcage.

When PFOA was exposed to the ReTTFcage, significant chemical shift changes were observed, while no such changes were noted when exposed to the TTFcage. Specifically, the -CF_2 peak near the carbonyl group of PFOA shifted towards the lower field, indicating a strong hydrogen bond interaction between ReTTFcage and PFOA.

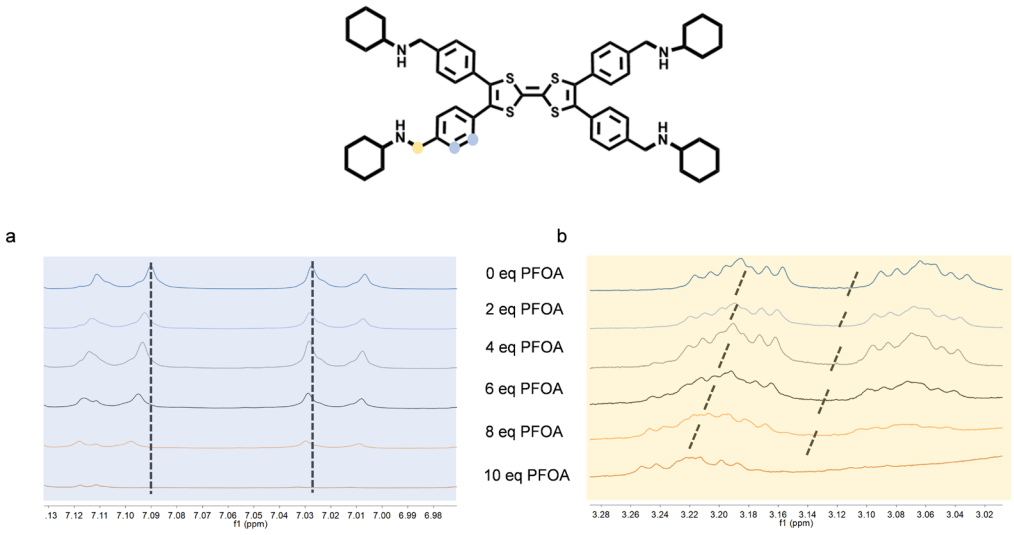

Figure S36. ^{1}H NMR titration of ReTTFcage at various PFOA concentrations in THF-*d8*.

It can be seen that the protons in the aromatic region of ReTTFcage and the methylene protons connected to nitrogen shift towards the low-field direction with the increase of PFOA concentration. These shifts are due to hydrogen bonds between the nitrogen site of the secondary amine bond and PFOA.

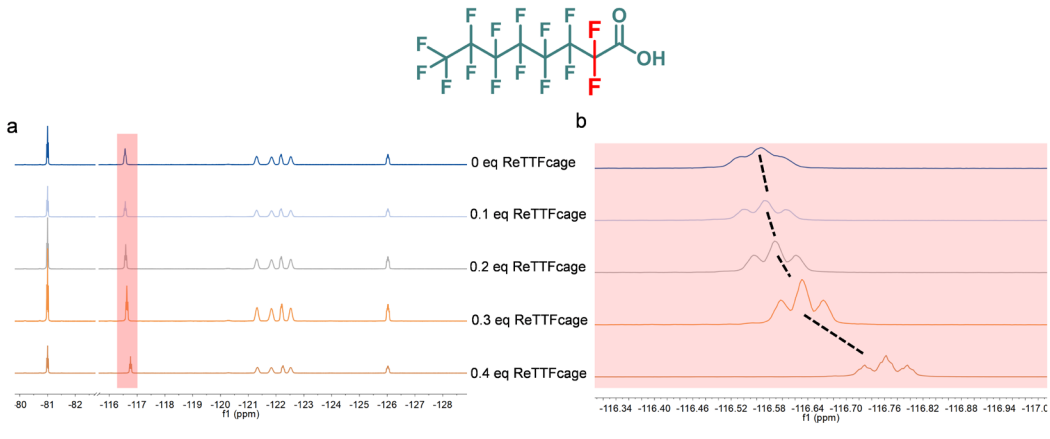

Figure S37. ^{19}F NMR titration of PFOA at various ReTTFcage concentrations in THF-*d8*.

It can be seen that as the concentration of ReTTFcage increases, the -CF_2 signal of the adjacent carboxyl groups in PFOA shifts towards the high-field direction. This discovery is consistent with the hydrogen bond conclusion between ReTTFcage and PFOA.

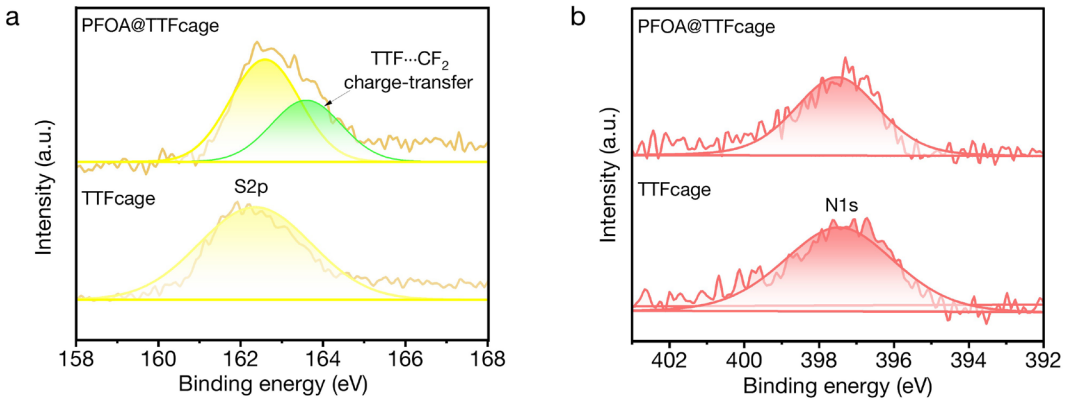

Figure S38. XPS analysis of a) S2p spectra and b) N1s spectra of TTFcage before and after PFOA uptake.

From the XPS analysis, it was found that XPS only gave an S2p peak shift due to the charge-transfer interactions but without obvious change on N1s peak. These means the lack of hydrogen bonding between TTFcage and PFOA.

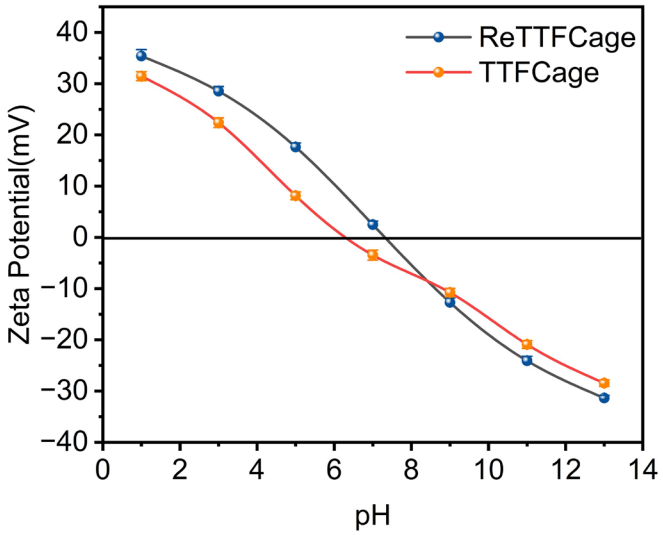

Figure S39. Zeta potential of ReTTFcage and TTFcage at different pH.

Zeta potential results show that ReTTFcage is more positively charged than TTFcage. Specifically, at pH < 7.3, ReTTFcage exhibits positive charge and has the potential to form electrostatic attraction with PFOA.

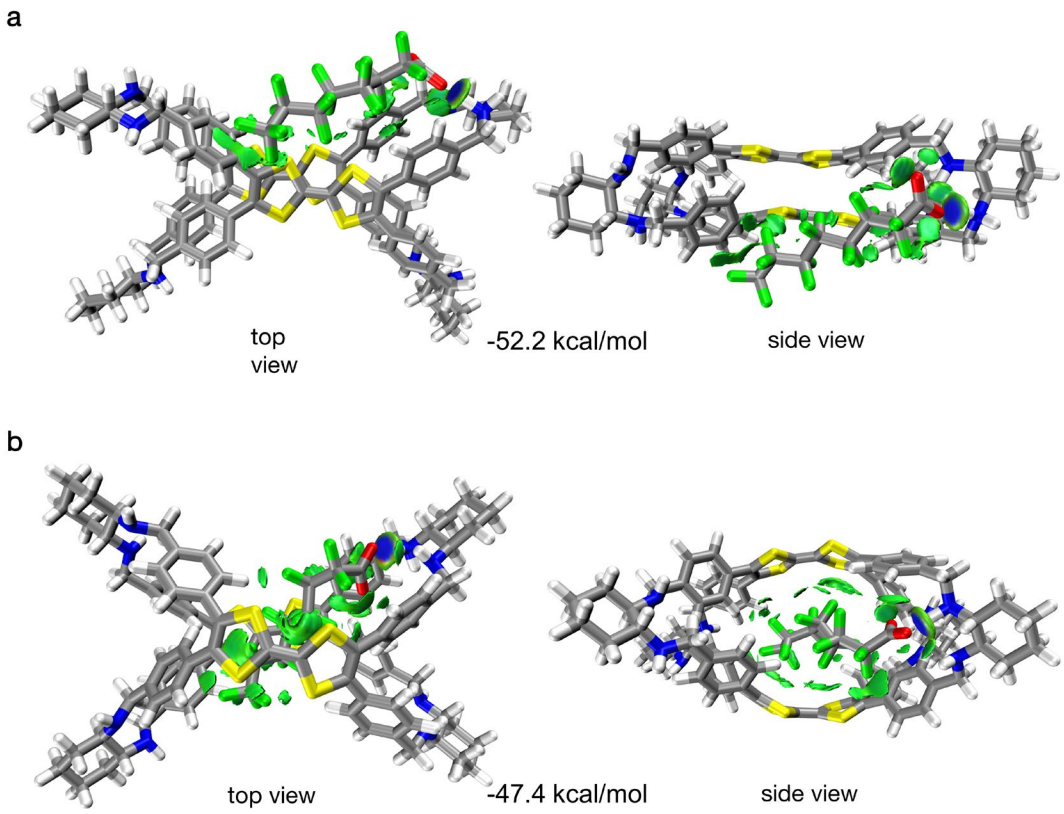

Figure S40. Independent gradient model (IGM) analysis of the binding interactions between ReTTFcage and PFOA in diverse binding motifs: one PFOA bound (a) outside and (b) in the cage.

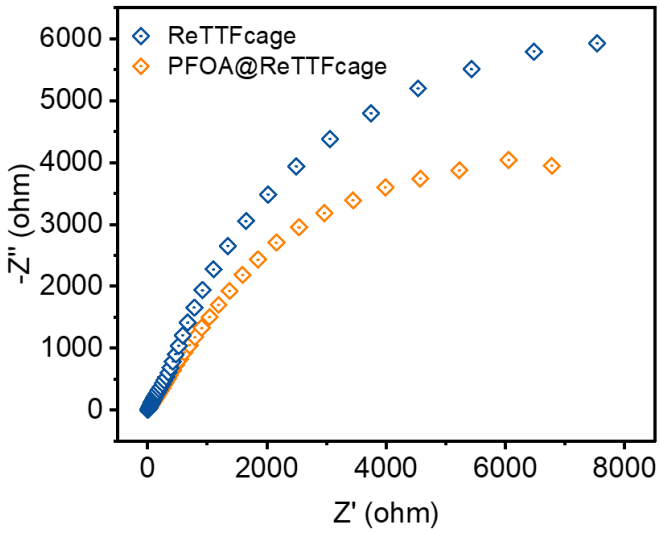

Figure S41. EIS analysis of ReTTFcage before and after PFOA uptake.

The Nyquist plot reveals a significantly reduced charge transfer resistance for the PFOA@ReTTFcage composite compared to the pristine ReTTFcage. This smaller impedance suggests that the encapsulation of PFOA facilitates faster electron transfer, which is evidence of enhanced interfacial conductivity.

References

1. Bannwarth, C., Ehlert, S. & Grimme, S. GFN2-xTB—an accurate and broadly parametrized self-consistent tight-binding quantum chemical method with multipole electrostatics and density-dependent dispersion contributions. *J. Chem. Theory Comput.* **15**, 1652-1671 (2019).

2. Grimme, S., Bannwarth, C. & Shushkov, P. A robust and accurate tight-binding quantum chemical method for structures, vibrational frequencies, and noncovalent interactions of large molecular systems parametrized for all spd-block elements (Z = 1-86). *J. Chem. Theory Comput.* **13**, 1989-2009 (2017).

3. Stephens, P. J., Devlin, F. J., Chabalowski, C. F. & Frisch, M. J. Ab initio calculation of vibrational absorption and circular dichroism spectra using density functional force fields. *J. Phys. Chem.* **98**, 11623-11627 (1994).

4. Frisch, M. J. *et al. Gaussian 16 Revision A.03* (Gaussian, Inc., Wallingford, CT, 2016).

5. Li, W. et al. AIE-active chiral [3]rotaxanes with switchable circularly polarized luminescence. *Angew. Chem. Int. Ed.* **60**, 9507-9515 (2021).

6. Grimme, S., Ehrlich, S. & Goerigk, L. Effect of the damping function in dispersion corrected density functional theory. *J. Comput. Chem.* **32**, 1456-1465 (2011).

7. Parker, T. M., Burns, L. A., Parrish, R. M., Ryno, A. G. & Sherrill, C. D. Levels of symmetry adapted perturbation theory (SAPT). I. efficiency and performance for interaction energies. *J. Chem. Phys.* **140**, 094106 (2014).

8. Lu, T. & Chen, F. Quantitative analysis of molecular surface based on improved marching tetrahedra algorithm. *J. Mol. Graph. Model.* **38**, 314-323 (2012).

9. Ilić, N. *et al.* Trace adsorptive removal of PFAS from water by optimizing the UiO-66 MOF interface. *Adv. Mater.* **37**, 2413120 (2025).

10. Zhang, Y. *et al.* A porphyrinic metal-organic framework with cooperative adsorption domains for PFAS removal from water. *ChemSusChem* **17**, e202400069 (2024).

11. Guo, H. *et al.* Roles of varying carbon chains and functional groups of legacy and emerging per-/polyfluoroalkyl substances in adsorption on metal-organic framework: insights into mechanism and adsorption prediction. *Environ. Res.* **251**, 118679 (2024).

12. Liang, R.-R. *et al.* Exceptionally high perfluorooctanoic acid uptake in water by a zirconium-based metal-organic framework through synergistic chemical and physical adsorption. *J. Am. Chem. Soc.* **146**, 9811-9818 (2024).

13. Liang, R.-R. *et al.* Zirconium-based metal-organic frameworks with free hydroxy groups for enhanced perfluorooctanoic acid uptake in water. *Adv. Mater.* **36**, 2407194 (2024).

14. Loukopoulos, E. *et al.* Chemically tailored metal-organic frameworks for enhanced capture of short- and long-chain per- and polyfluoroalkyl substances from water. *Adv. Funct. Mater.* **34**, 2409932 (2024).

15. Yang, Y.-Q., Zheng, Z.-H., Ji, W.-Q. & Xu, J. C. Insights to perfluorooctanoic acid adsorption micro-mechanism over Fe-based metal organic frameworks: combining computational calculation with response surface methodology. *J. Hazard. Mater.* **395**, 122686 (2020).

16. Yin, H.-Q. *et al.* A switchable sensor and scavenger: detection and removal of fluorinated chemical species by a luminescent metal-organic framework. *Chem. Sci.* **12**, 14189-14197 (2021).

17. Huang, J. *et al.* Metal-organic framework-based fluorescent sensor array for discriminating and detecting per- and polyfluoroalkyl substances. *Adv. Funct. Mater.* **32**, 2203171 (2022).

18. Tang, H.-Z. *et al.* Self-assembled stable magnetic COF super-particles through electrostatic interaction for efficient removal and detection of PFAS combined with LC-MS/MS. *Adv. Funct. Mater.* **35**, e12313 (2025).

19. Jrad, A. *et al.* Cationic covalent organic framework for the fluorescent sensing and cooperative adsorption of perfluorooctanoic acid. *Nat. Commun.* **15**, 10490 (2024).

20. Zadehnazari, A., Khosropour, A., Zarei, A., Khazdooz, L., Amirjalayer, S. & Abbaspourrad, A. Sustainable phenolic polymer networks embedded with β-cyclodextrin for the efficient capture of per- and polyfluoroalkyl substances from water. *Small* **20**, 2405176 (2024).

21. Zarei, A. *et al.* β-Cyclodextrin-phenolic polymer networks with tunable porosity for the enhanced adsorption and detection of per- and polyfluoroalkyl substances. *ACS*

Appl. Mater. Interfaces **16**, 9483-9494 (2024).

22. Zarei, A. *et al.* Mechanistic study of PFAS adsorption using a QPPTA linked viologen-modified covalent organic framework. *J. Mater. Chem. A* **13**, 8180-8192 (2025).

23. Zeppuhar, A. N. *et al.* Linkage transformations in a three-dimensional covalent organic framework for high-capacity adsorption of perfluoroalkyl substances. *ACS Appl. Mater. Interfaces* **15**, 52622-52630 (2023).

24. He, Y. *et al.* Amplified fluorescence detection of ultratrace PFAS in water using fluorinated conjugated polymers bearing pyridyl selectors. *J. Am. Chem. Soc.* **146**, 6225-6230 (2024).

25. He, Y. *et al.* Porous adaptive luminescent metallacage for the detection and removal of perfluoroalkyl carboxylic acids. *Chem* **9**, 93-101 (2023).

26. Mu, C. Q. *et al.* Pyrene-based covalent organic frameworks with hydrophobic and electrostatic dual interaction sites for efficient adsorption of short-chain perfluoroalkyl substances. *ACS Nano* **19**, 37943-37953 (2025).

27. Camdzic, D. *et al.* Rapid capture of per- and polyfluoroalkyl substances using a self-assembling zirconium-based metal-organic cage. *ACS Appl. Eng. Mater.* **2**, 87-95 (2024).

28. Pérez-Ferreiro, M., Gallagher, Q. M., Webb, M. A. & Criado, A. Computational and experimental insights into the adsorption of perfluoroalkyl substances on a mesoporous zirconium-based metal-organic framework. *J. Mater. Chem. A* **13**, 24466-24472 (2025).

29. Chen, Z. H. *et al.* Efficient recognition and removal of persistent organic pollutants by a bifunctional molecular material. *J. Am. Chem. Soc.* **145**, 260-267 (2023).

30. Liu, X.-L. *et al.* Synergistic binding sites in porous aromatic frameworks for highly efficient perfluorooctanoic acid removal. *Nat. Commun.* **13**, 2132 (2022).

31. Xiao, L. L. *et al.* β-Cyclodextrin polymers with different cross-linkers for sorption of PFAS byproducts from water. *J. Am. Chem. Soc.* **139**, 7689-7692 (2017).

32. Chaix, A. *et al.* Polymer nanoparticles with a hydrophobic core and cationic shell for the efficient removal of per- and polyfluoroalkyl substances from water. *Adv. Mater.* **37**, 2410720 (2025).

33. Fu, K. X. *et al.* Amphipathic fluoroamine-functionalized hydrogels for enhanced selective removal of anionic PFAS from water. Nat. Commun. 16, 10152 (2025).

34. Chen, W., Zhang, X. P., Mamadiev, M. & Wang, Z. H. Sorption of perfluorooctane sulfonate and perfluorooctanoate on polyacrylonitrile fiber-derived activated carbon fibers: in comparison with activated carbon. *RSC Adv.* **7**, 927-938 (2017).

35. Yang, Z. *et al.* Toward standardized evaluation of PFAS sorbents. *Adv. Mater.* **38**, e202516944 (2026).

36. Sun, Y. J., Pérez-Padilla, V., Valderrey, V., Bell, J. & Gawlitza, K. Ratiometric detection of perfluoroalkyl carboxylic acids using dual fluorescent nanoparticles and a miniaturised microfluidic platform. *Nat. Commun.* **16**, 10869 (2025).

37. Concellón, A., Castro-Esteban, J. & Swager, T. M. Fluorous-fluorous interactions amplify the detection of perfluorinated alkyl substances using semiconducting polymers. *J. Am. Chem. Soc.* **145**, 11420-11430 (2023).

38. Dong, C.-C. *et al.* Side-chain engineering of polythiophene probes for multimodal discrimination of PFAS via conformational switching. *Angew. Chem. Int. Ed.* **65**, e21236 (2025).

39. Dalapati, R., Hunter, M., Mostakim, S. K., Yang, X. M. & Zang, L. Fluorescence turn-on detection of perfluorooctanoic acid (PFOA) by perylene diimide-based metal-organic framework. *ACS Appl. Mater. Interfaces* **16**, 32344-32356 (2024).

40. Zhang, Q. *et al.* Dual-mode ratiometric fluorescent and smartphone-readable sensor based on N, S-co-doped carbon dots for ultrasensitive detection of perfluorooctanoic acid. *Anal. Chem.* **97**, 26108-26117 (2025).

41. Yang, N. *et al.* Reagent-free multicolor colorimetric sensor for PFAS based on oxidation-aggregation coupling of gold nanoclusters. *Microchim. Acta* **192**, 134 (2025).

42. Cui, Y. *et al.* Paper-based electrochemical sensor integrated with molecularly imprinted polymer for selective detection of perfluorooctanoic acid. *Microchim. Acta* **192**, 356 (2025).

43. Zheng, X. *et al.* Reagent-free multicolor colorimetric sensor array for PFAS discrimination based on aggregation-oxidation coupling of gold nanoclusters and smartphone readout. *Anal. Chem.* **97**, 6347-6358 (2025).

44. Roh, H. *et al.* Copper-based two-dimensional conductive metal-organic framework thin films for ultrasensitive detection of perfluoroalkyls in drinking water. *ACS Nano* **19**, 6332-6341 (2025).

45. Tian, Q. Y. *et al.* ZIF-8-derived hollow ZnO@ZIF-67 core-shell heterostructure film for the ultrasensitive chemiresistive detection of perfluorooctanoic acid. *Sens. Actuators B Chem.* **404**, 135309 (2024).

46. Huerta, B., McHugh, B. & Regan, F. Development and validation of a SPE-LC-MS/MS method for the determination of per- and polyfluoroalkyl substances (PFAS) in drinking water and surface water. *Anal. Methods* **14**, 2090-2099 (2022).